

SUBARU WEAK-LENSING SURVEY OF DARK MATTER SUBHALOS IN THE COMA CLUSTER: SUBHALO MASS FUNCTION AND STATISTICAL PROPERTIES*

NOBUHIRO OKABE^{1,2}, TOSHIFUMI FUTAMASE³, MASARU KAJISAWA⁴, AND RISA KUROSHIMA³

¹ Kavli Institute for the Physics and Mathematics of the Universe (WPI), Todai Institutes for Advanced Study,

University of Tokyo, 5-1-5 Kashiwanoha, Kashiwa, Chiba 277-8583, Japan; nobuhiro.okabe@ipmu.jp

² Institute of Astronomy and Astrophysics, Academia Sinica, P.O. Box 23-141, Taipei 106, Taiwan

³ Astronomical Institute, Tohoku University, Sendai 980-8578, Japan

⁴ Research Center for Space and Cosmic Evolution, Ehime University, Bunkyo-cho 2-5, Matsuyama 790-8577, Japan

Received 2013 April 8; accepted 2014 February 4; published 2014 March 7

ABSTRACT

We present a 4 deg² weak gravitational lensing survey of subhalos in the very nearby Coma cluster using the Subaru/Suprime-Cam. The large apparent size of cluster subhalos allows us to measure the mass of 32 subhalos detected in a model-independent manner, down to the order of 10⁻³ of the virial mass of the cluster. Weak-lensing mass measurements of these shear-selected subhalos enable us to investigate subhalo properties and the correlation between subhalo masses and galaxy luminosities for the first time. The mean distortion profiles stacked over subhalos show a sharply truncated feature which is well-fitted by a Navarro–Frenk–White (NFW) mass model with the truncation radius, as expected due to tidal destruction by the main cluster. We also found that subhalo masses, truncation radii, and mass-to-light ratios decrease toward the cluster center. The subhalo mass function, $dn/d \ln M_{\text{sub}}$, in the range of 2 orders of magnitude in mass, is well described by a single power law or a Schechter function. Best-fit power indices of $1.09^{+0.42}_{-0.32}$ for the former model and $0.99^{+0.34}_{-0.23}$ for the latter, are in remarkable agreement with slopes of ~ 0.9 – 1.0 predicted by the cold dark matter paradigm. The tangential distortion signals in the radial range of 0.02–2 h^{-1} Mpc from the cluster center show a complex structure which is well described by a composition of three mass components of subhalos, the NFW mass distribution as a smooth component of the main cluster, and a lensing model from a large scale structure behind the cluster. Although the lensing signals are 1 order of magnitude lower than those for clusters at $z \sim 0.2$, the total signal-to-noise ratio, $S/N = 13.3$, is comparable, or higher, because the enormous number of background source galaxies compensates for the low lensing efficiency of the nearby cluster.

Key words: galaxies: clusters: individual (Coma Cluster (A1656)) – gravitational lensing: weak – X-rays: galaxies: clusters

Online-only material: color figures

1. INTRODUCTION

The cold dark matter (CDM) concordance cosmology has had considerable success in explaining various observations on a large scale, such as the cosmic microwave background (Komatsu et al. 2011; Hinshaw et al. 2013). It provides initial conditions for the hierarchical structure formation involved in the mass assembly histories of halos, for high-resolution N -body simulations and analytical models. In hierarchical clustering, less massive halos are accreted into more massive halos, which are then subsequently eroded by effects combined with tidal stripping and dynamical friction of the host halo, eventually becoming a smooth component. Since galaxy clusters are the most massive virialized objects in the universe, the central regions of subhalos have survived under the over-density field until the recent epoch, and constitute their population. Numerical simulations of, and analytic approaches to CDM predict that subhalo mass functions at the intermediate and low mass scales follow a power law, $dn/d \ln M_{\text{sub}} \propto M_{\text{sub}}^{-\alpha}$ with slopes of ~ 0.9 – 1.0 (e.g., Taylor & Babul 2004, 2005a, 2005b; Oguri & Lee 2004; van den Bosch et al. 2005; Diemand et al. 2004; De Lucia et al. 2004; Gao et al. 2004b, 2012; Shaw et al. 2006; Angulo et al. 2009; Giocoli et al. 2010; Klypin et al. 2011; Wu et al. 2013).

Observations of cluster subhalo properties, such as mass function and spatial distribution, provide us with a deeper understanding of the mass assembly history and are the most stringent test of CDM predictions on scales of less than several Mpc. A characteristic feature of the subhalo mass function is also critically important to constrain the nature of dark matter, because it depends on the particle mass of dark matter. Furthermore, a study of the correlation between galaxy properties and subhalo masses, incorporating different data-sets, sheds important insight on the physics of galaxy evolution associated with dark matter. Thus, it is of paramount importance to measure the mass function directly from observations without assuming a relationship between dark matter and luminous matter and the dynamical state of the system. It is difficult, though, to infer the masses of subhalos from visible matter, such as galaxies, because assumptions about the mass distribution extending beyond galaxies and dynamical state of the galaxies are required. In this situation, weak gravitational lensing analysis plays an important role. Weak lensing analysis measures a coherent distortion pattern of background galaxy images caused by the gravitational field of the system and thus avoids any of the assumptions mentioned above (e.g., Bartelmann & Schneider 2001). However, the weak-lensing signal is obtained by averaging over a certain number of background galaxies, and thus, only the mass information over a scale of several arcminutes is obtained. Previous weak lensing studies or joint strong- and weak-lensing studies (Broadhurst et al. 2005; Okabe et al. 2010b, 2011,

* Based on data collected from the Subaru Telescope and obtained from SMOKA, operated by the Astronomy Data Center, National Astronomical Observatory of Japan.

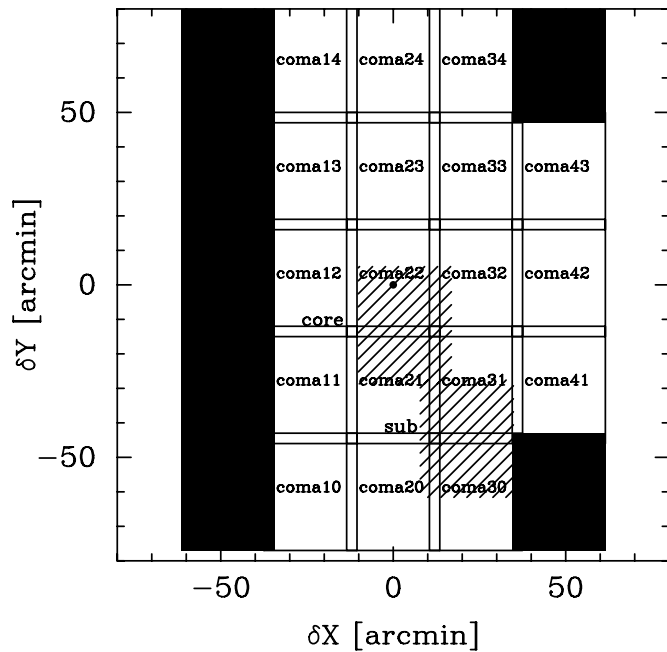


Figure 1. Cadence design for the Coma cluster subhalo survey. The horizontal and vertical axes are R.A. and decl. with an offset distance from NGC 4874, in units of arcmin. The data set name (Table 1) is indicated in the middle of each pointing. The pointings have an overlap of 2 arcmin, with a total survey area of 4.1 deg^2 . Hatched regions represent areas of archival data (core and sub). A summary of the imaging data is shown in Table 1.

2013; Oguri et al. 2010, 2012; Umetsu & Broadhurst 2008; Umetsu et al. 2010, 2011; Applegate et al. 2012; Hoekstra et al. 2012) mainly focused on clusters at redshift higher than approximately 0.15, because of good lensing efficiency and high-quality imaging data obtained using wide-field cameras mounted on ground-based telescopes, such as the Subaru Prime Focus Camera (Suprime-Cam; Miyazaki et al. 2002) on the 8.2m Subaru Telescope. However, it is very difficult to detect subhalos using weak lensing analysis of clusters at $z \sim 0.2$ with masses on the order of $10^{12} h^{-1} M_{\odot}$, because the apparent truncation size ($\sim 0.2\text{--}0.5$ or less) of these subhalos is too low to be detected in the lensing signal. Stacking lensing studies for member galaxies help to overcome this disadvantage (Natarajan & Springel 2004; Natarajan et al. 2007, 2009; Limousin et al. 2005, 2007). It computes lensing distortion signals centered around member galaxies and, thus, is independent of lensing selections, which increases an signal-to-noise ratio (S/N) in lensing signals due to the large sample size. Hence, the stacking analysis enables us to measure a mean mass of subhalos associated with member galaxies. However, a correlation between the luminosity and mass of the subhalos must be assumed to derive a subhalo mass function and/or conduct statistical studies of subhalos.

Weak-lensing studies of very nearby clusters ($z \lesssim 0.1$) overcome the problems described above. In contrast to weak-lensing studies of clusters at $z \sim 0.2$, there are three significant advantages in the analysis of dark matter subhalos. First, a large apparent size enables us to easily resolve less massive subhalos inside the clusters. Second, subhalos are sufficiently separated from the main cluster center and other subhalos to ignore their lensing contamination in subhalo mass measurements. Third, a large angular scale provides a correspondingly large number of background galaxies, which leads to low statistical errors and compensates for low lensing efficiency to achieve a high S/N. This last advantage also plays an important role in cluster

Table 1
Imaging Data

Name ^a	R_c ^b (min)	V ^b (min)	Seeing ^c (arcsec)	\bar{r}_h^{*d} (arcsec)
coma10	24.5	13.75	0.93	0.48
coma11	24.5	13.75	0.65	0.34
coma12	24.5	13.75	0.63	0.32
coma13	24.5	13.75	0.63	0.31
coma14	24.5	13.75	0.65	0.33
coma20	24.5	14.75	0.75	0.39
coma21	24.5	13.75	0.59	0.29
coma22	24.5	13.75	0.75	0.39
coma23	24.5	13.75	0.63	0.33
coma24	24.5	13.75	0.57	0.28
coma30 ^e	24.5	13.92	0.69	0.36
coma30 ^f	24.5	13.92	0.67	0.35
coma31	24.5	13.75	0.61	0.30
coma32	24.5	13.75	0.71	0.37
coma33	24.5	13.75	0.83	0.54
coma34	24.5	13.75	0.70	0.36
coma41	24.5	14.58	0.72	0.38
coma42	24.5	14.58	0.72	0.38
coma43	24.5	13.75	0.76	0.40
core ^g	42.0	...	0.81	0.41
sub ^g	16.0	...	0.83	0.41

Notes.

^a Data set.

^b Exposure times in R_c and V bands, respectively.

^c The seeing FWHM in unit of arcseconds, for R_c band.

^d The median stellar half-light radius in unit of arcseconds, for R_c band.

^e R_c band data taken in 2011 March 1.

^f R_c band data taken in 2011 March 30.

^g Data retrieved from SMOKA.

mass measurements. For example, the Coma cluster is at redshift $z_c = 0.0236$, with a large apparent size ~ 7 times larger than that of clusters at $z \sim 0.2$. We thus use the area of 50–100 square minutes or more in weak-lensing mass measurements of subhalos with masses greater than $\sim 10^{12} h^{-1} M_{\odot}$. Indeed, Okabe et al. (2010a) has demonstrated the power of weak-lensing analysis of the Coma cluster and discovered less massive subhalos.

Here we report the results of a 4.1 deg^2 weak gravitational lensing survey of subhalos in the Coma cluster by 18 pointing observations (R_c and V bands) using the Subaru/Suprime-Cam to directly measure subhalo masses and their mass function. This paper is a continuation of our previous work (Okabe et al. 2010a), which used archival Subaru/Suprime-Cam data with the R_c band. The archival data covers the central and the southwest regions (two pointings; see also Figure 1), with a total area of $\sim 0.5 \text{ deg}^2$. Our new data significantly improves the quality of the weak-lensing analysis. First, the data covers an area to the outskirts of the cluster, which enables us to study the radial dependence of subhalo properties. Area fractions, for the previous and new data, respectively, account for $\sim 10\%$ and $\sim 80\%$ within r_{200} inside of which the mean interior density is 200 times the critical mass density at the cluster redshift. Second, the exposure time is deeper than the effective one used in the previous weak-lensing analysis (~ 16 minutes; Table 1), which increases the number of background galaxies and thus suppresses the noise for the intrinsic ellipticity. Third, we used two filters to secure the background galaxies, avoiding contamination of unlensed member/foreground galaxies in our shear catalog. Therefore, this new data enables us to conduct a systematic survey for cluster subhalos for the first time. We

describe the details of data analysis in Section 2, including shape measurements, background and member selections and modeling of background lensing signals. In Section 3, we define the subhalos from lensing signals, measure model-independent projected mass, conduct stacked lensing analyses and evaluate systematic errors including the purity of the subhalo sample. We also present a galaxy–galaxy lensing study for luminous member galaxies in Section 4, which is complementary to and independent of the analyses in Section 3. We describe measurement of the main cluster mass in Section 5. Finally, we discuss the subhalo mass function, subhalo properties, and future studies in Section 6. The conclusions are stated in Section 7. Throughout this paper, we use the cosmology of $\Omega_{m0} = 0.27$, $\Omega_{\Lambda} = 0.73$ and $H_0 = 100 h \text{ km s}^{-1} \text{ Mpc}^{-1}$. One arcmin corresponds to $20 h^{-1} \text{ kpc}$.

2. DATA ANALYSIS

2.1. Survey Observation and Image Processing

We observed the Coma cluster using the Suprime-cam (Miyazaki et al. 2002) at the Subaru 8.2-m telescope, in R_c and V bands, in 2011 March and April. The R_c band data is used for the wide-field weak lensing analysis, and combined with V band data to minimize contamination of the member and foreground galaxies in the shear catalog. The survey is covered by a mosaic of 18 pointings, specifically, coma10...coma43, as shown in Figure 1. Each pointing overlaps by 2 arcmin. The total survey area is 4.1 deg^2 . A maximum projected radius from the brightest cluster galaxy, NGC 4874, reached $\sim 100'$ which is comparable to the cluster virial radius r_{vir} (Section 5). The R_c band data of coma30 was recollected due to the low number of background galaxies. The typical exposure times for R_c and V bands are 24.5 and ~ 14.0 minutes (Table 1). We also used two R_c imaging data sets retrieved from Subaru archival data (SMOKA⁵).

We used the standard pipeline reduction software for the Suprime-Cam, SDFRED (Yagi et al. 2002; Ouchi et al. 2004) modified for the new CCD, for flat-fielding, instrumental distortion correction, differential refraction, point-spread-function (PSF) matching, sky subtraction and stacking. The seeing for each pointing is shown in Table 1. An astrometric calibration was performed using point sources from the Two Micron All Sky Survey catalog (Skrutskie et al. 2006). The typical residual values are no larger than the CCD pixel size. Photometric calibration was carried out by fitting point sources detected in each data set with stars from Sloan Digital Sky Survey (SDSS) DR8 photometry (Eisenstein et al. 2011), taking into account the difference between their sensitivities. The archival data obtained using the previous CCDs was reduced by the same procedure using the SDFRED for the previous CCDs.

2.2. Weak Lensing Distortion Analysis

The weak lensing measurements follow Kaiser et al. (1995), referred to as the KSB+ method, which uses the IMCAT package with some modifications, similar to Umetsu et al. (2010), Oguri et al. (2012), Okabe et al. (2013). Image ellipticity is measured from the weighted quadrupole moments of the surface brightness of objects detected in the R_c band imaging data (Table 1). The anisotropic PSF correction is conducted in the same manner as Okabe et al. (2010a, 2010b, 2011, 2013). We select bright unsaturated stars in the half-light radius, r_h , and magnitude plane to estimate the stellar anisotropy kernel,

$q_{\alpha}^* = (P_{\text{sm}}^*)^{-1}_{\alpha\beta} e_{\alpha}^*$, where $P_{\text{sm}}^{\alpha\beta}$ is the smear polarizability matrix, and e_{α} is the image ellipticity. Quantities with an asterisk denote those for stellar objects. Following the KSB method, PSF anisotropy is corrected with the equation

$$e'_{\alpha} = e_{\alpha} - P_{\text{sm}}^{\alpha\beta} q_{\beta}^*. \quad (1)$$

We estimate $q_{\alpha}^{\alpha}(\theta)$ at each galaxy position, θ , using a fitting function of second-order bi-polynomials of the vector θ with iterative σ -clipping rejection. The data region is then divided into several rectangular blocks based on the typical coherent scale of the measured PSF anisotropy pattern. A number of tests were performed to assess the anisotropic PSF correction (see details in Appendix A). To estimate systematic residuals caused by imperfect PSF correction, we computed an auto-correlation function for the stellar ellipticities and a cross-correlation function for the ellipticities of galaxies and stars, before and after the correction, respectively. Although the autocorrelation and the cross-correlation functions for raw ellipticities before the correction are highly corrected to the order of 10^{-5} – 10^{-4} , the residual/corrected ellipticities show no correlation, which supports the accuracy of the anisotropic PSF correction.

Next, the isotropic smearing effect of galaxy images is corrected to estimate the reduced distortion signal, g_{α} ,

$$g_{\alpha} = (P_g^{-1})_{\alpha\beta} e'_{\beta}, \quad (2)$$

where $P_{\alpha\beta}^g$ is the pre-seeing shear polarizability tensor. The measurement of $P_{\alpha\beta}^g$ is very noisy for individual faint galaxies because of its nonlinearity (Bartelmann & Schneider 2001), which may result in a systematic bias in weak-lensing distortion measurements. We therefore calibrate $P_{\alpha\beta}^g$ using the following procedures, in a similar way as Umetsu et al. (2010) and Oguri et al. (2012). The polarizability tensor is first computed as a scalar polarizability, $(P_g)_{\alpha\beta} = (1/2)\text{tr}[P_g]\delta_{\alpha\beta}$. We then compute a median for $(P_g)_{\alpha\beta}$ in r_g , with an adaptive grid to assemble as uniformly as possible. Here, r_g is the Gaussian smoothing radius used in the KSB method. A sample of galaxies satisfies the following conditions to suppress the noise: a detection significance level of $\nu > 30$, a size condition of $r_h > \bar{r}_h^* + \sigma(r_h^*)$ and $r_g > \bar{r}_g^* + \sigma(r_g^*)$ and a positive raw P_g . Here, \bar{r}_h^* ($\sigma(r_h^*)$) and \bar{r}_g^* ($\sigma(r_g^*)$) are the median (rms dispersion) of half-light radii and Gaussian smoothing radii for the stars selected above. We interpolate the polarizability tensor for individual galaxies as a function of r_g . A similar interpolation for the absolute value of the ellipticity, $|e|$, is also applied. We use galaxies for the shear catalog with $\nu > 10$ and the same size cut as in the calibration. An rms error of the shear estimate, σ_g , is computed from 50 neighbors in the magnitude- r_g plane. We also assign the weight function for individual objects.

$$w_g = \frac{1}{\sigma_g^2 + \alpha^2} \quad (3)$$

where α is the softening constant variance representing the scatter due to the intrinsic ellipticity of the galaxies (e.g., Hoekstra et al. 2000; Hamana et al. 2003; Okabe et al. 2010b; Umetsu et al. 2010; Oguri et al. 2012). We choose $\alpha = 0.4$, which is a typical value of the mean rms σ_g over the background sample. In the limit of $\sigma_g \ll \alpha$, individual galaxies are uniformly weighted. On the other hand, noisy objects, such as fainter objects, are less weighted.

To check shear calibration, we use a number of realistic images for which the field-of-view is comparable to the

⁵ <http://smoka.nao.ac.jp/index.jsp>

Subaru/Suprime-cam (kindly provided by M. Oguri). The mock images are generated with different seeing sizes (0.5–1.1 arcsec) and the Moffat profile with power slopes $3 < \beta < 12$, using GLAFIC software (Oguri 2010), as described in Oguri et al. (2012). We found that a multiplicative calibration bias, m and an additive residual shear offset, c in Heymans et al. (2006) and (Massey et al. 2007) are $|m| \lesssim 0.03$ and $|c| \lesssim 2 \times 10^{-4}$, respectively, for our typical seeing $\sim 0''.7$.

We then combine the shear catalog constructed from individual images. For the overlapping regions, since the same galaxies are detected in different images, we estimate weighted averages of their position and shear with w_g . We compared reduced shear for 1.8×10^5 overlapping galaxies and confirmed that the deviation, $\Delta g_\alpha = (-2.16 \times 10^{-6} \pm 6.6 \times 10^{-4}, 1.93 \times 10^{-6} \pm 6.6 \times 10^{-4})$, is negligible. Using this approach, the number of background galaxies is $\sim 6.7 \times 10^5$.

2.3. Photometry and Background Selection

A secure selection of background galaxies in the color–magnitude plane was used because contamination by unlensed member or foreground galaxies in the shear catalog dilutes the weak-lensing signals, leading to an underestimation of the gravitational lensing mass, mainly for the central regions (Broadhurst et al. 2005; Okabe et al. 2010b, 2013).

Photometric catalogs were constructed from the mosaic images using SExtractor (Bertin & Arnouts 1996). The SExtractor parameters are optimized for faint galaxies for shape measurements. We compute the total magnitude for each object in the AB-magnitude system using the MAG_AUTO parameter and color using the MAG_APER parameter. For the color measurements, we degraded the seeing to the worst image. The aperture diameter for the MAG_APER parameter is 1.5 times the seeing FWHM. The overlapping galaxies serve as a monitor of the offset in the magnitude. We introduced an additional parameter in each data field to describe the offset using two magnitudes and calibrated them simultaneously fitting bright objects with magnitudes less than 22 mag. The measurement scatter for faint galaxies ($R_c > 24$ mag) is typically less than 0.1 mag. The magnitudes and colors for objects are estimated using weighting measurement errors. We then match the shear and SExtractor catalogs.

The red-sequence of member galaxies is fitted to a linear function, using luminous galaxies ($R_c < 18$ mag). We then define the background galaxies with colors redder than the red-sequence in the magnitude range of $20 \text{ mag} < R_c < 26 \text{ mag}$ (Figure 2). The number of background galaxies is reduced to $\sim 6 \times 10^5$ after the color cut but remains 30–60 times higher than those of clusters at $z \sim 0.2$, obtained by previous studies using two path-band filters (Okabe et al. 2010b). The number density, $n_g \simeq 41.3 \text{ arcmin}^{-2}$, is also from two to eight times higher than both those for clusters at $z \sim 0.2$, and for our previous analysis of the Coma cluster (Okabe et al. 2010a, $n_g \simeq 23 \text{ arcmin}^{-2}$). Thus, we can use a correspondingly large number of background source galaxies for nearby cluster weak-lensing analysis, for the following two reasons. First, since the colors of red-sequence galaxies in clusters becomes more blue with decreasing redshifts, the number of galaxies, with colors are redder than those of member galaxies, increases. Second, the large area encompassed by the nearby cluster increases the number of background galaxies. Even if member galaxies are contained in the background catalog, the dilution effect in lensing signals could be ignored because the ratio of thousands of member galaxies to the millions of background galaxies is

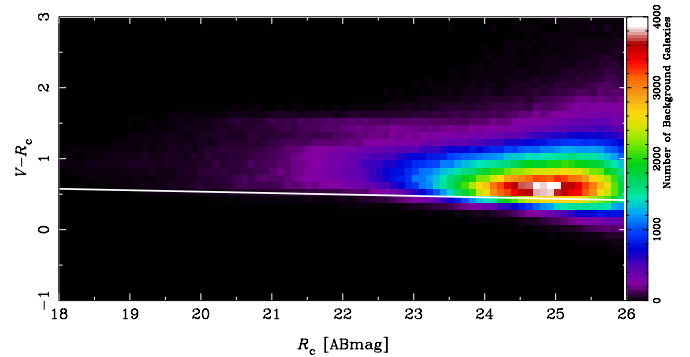


Figure 2. Color–magnitude diagram. The color shows the number of background galaxies in each pixel (0.1×0.1). The white solid line denotes the red-sequence of member galaxies, fitted to a linear function for the bright galaxies.

(A color version of this figure is available in the online journal.)

negligible. Thus, weak-lensing analysis of a nearby cluster has a great advantage to compensate for low-lensing efficiency.

2.4. Mean Lensing Depth

Since the redshifts of individual galaxies in the shear catalog are not available, we estimated the mean source redshift using a statistical approach. The lensing signal depends on the source redshifts through the distance ratio. As a reference, we used the COSMOS photometric redshift catalog (Ilbert et al. 2009) estimated by combining 30 broad, intermediate and narrow bands. Because the R_c band is not available in the COSMOS catalog, and we converted magnitudes from R_c to i' bands, based on the filter sensitivities of the Suprime-Cam. The probability function of redshift, dP_{WL}/dz , for our background galaxies selected by the color–magnitude plane (Section 2.3) is computed by matching with the COSMOS photometric redshift, with a statistical weight of w_g . The mean distance ratio is given by

$$\langle D_{\text{ls}}/D_s \rangle = \int_{z_c} dz dP_{\text{WL}}/dz D_{\text{ls}}/D_s, \quad (4)$$

where D_s and D_{ls} are the angular diameter distance to the sources and between the cluster (lens) and the sources, respectively. We obtain $\langle D_{\text{ls}}/D_s \rangle = 0.9554$. The mean source redshift, $\langle z_s \rangle = 0.61$, is slightly lower than that ($\langle z_s \rangle \sim 0.7\text{--}0.8$) for clusters at $z \sim 0.2$ (Okabe et al. 2013), because we include many background galaxies at lower redshifts. The mass estimate for nearby systems do not strongly depend on the redshift distribution of background sources.

2.5. Luminous Member Galaxies

We defined luminous member galaxies identified in spectroscopic observations in order to compare the mass properties. Luminous galaxies with a magnitude brighter than $i' < 18$ mag, were retrieved from SDSS DR8 (Eisenstein et al. 2011), in a $4 \times 4 \text{ deg}^2$ region centered on NGC 4874. Furthermore, member galaxies were selected within the redshift range of $|z - z_c| < \sigma_v(1 + z_c)/c$ and $\sigma = 3000 \text{ km s}^{-1}$, where c is the velocity of light. To complete the catalog of member galaxies on the bright end, we also checked the redshifts of galaxies in NED.⁶ If they satisfied the above conditions, they were added to the catalog. Luminosities of individual galaxies are estimated from apparent magnitudes using the k-correction for early-type galaxies, assuming a single redshift of z_c .

⁶ <http://ned.ipac.caltech.edu/>

2.6. Model of LSS Lensing

Weak-lensing mass measurements for clusters at low redshift suffer from lensing signals of background galaxies between the cluster and the source redshifts, referred to as uncorrelated large-scale structure (LSS) lensing. The three-dimensional, inhomogeneous mass distribution causes a locally strong shear pattern, which potentially gives biases in detection and mass measurements of localized objects, such as subhalos. We therefore quantified the uncorrelated LSS lensing effect on each galaxy in the shear catalog, using the luminosity and photometric redshift retrieved from SDSS DR8 (Eisenstein et al. 2011), following Okabe et al. (2010a). Galaxies are selected with magnitudes $i' < 24$ mag and photometric redshifts between the cluster, $z_{\text{ph}} - z_c > \delta z = \sigma_v(1 + z_c)/c \simeq 0.01$, and the source redshift, where z_{ph} is the photometric redshift of each galaxy. Galaxies spectroscopically identified as member galaxies (Section 2.5) were excluded. Masses of individual galaxies are estimated using galaxy–galaxy lensing results from SDSS data Guzik & Seljak (2002). Using the mass-to-light ratio in each band ($u'g'r'i'z'$) derived by stacked lensing analysis of galaxies, the luminosity is converted into the mass. The masses estimated with different bands are used to cross-check and calibrate systematic errors in the mass–luminosity scaling relation utilized here. Since uncorrelated LSS lensing is obtained by integrating the effect of light deflections due to galaxies at different redshifts along the line-of-sight, the best-fit scaling relations in mass estimates for individual objects were used in order to quantify an average LSS lensing effect. The interior mass profile of each halo is assumed to be a universal mass profile found in numerical simulations, referred to as Navarro–Frenk–White (NFW; Navarro et al. 1996, 1997). The NFW mass model is described by two parameters: the mass and concentration (see details in Appendix D). It is well known that there is a correlation between mass and halo concentration (Bullock et al. 2001) predicted by the hierarchical structure formation scenario. We use the mass-concentration relation obtained from recent numerical simulations based on *WMAP5* cosmology parameters (Duffy et al. 2008) to describe the internal structure. The tangential distortion signals of individual galaxies are computed on all source galaxies. We found that the shear estimated in the r' band is consistent with that in the z' band, but the estimates in the $u'g'r'i'z'$ bands are systematically different, as found in Okabe et al. (2010a). The LSS lensing model based on the galaxy–galaxy lensing result is therefore defined with $g_{\alpha}^{(\text{LSS})} = (g_{\alpha}^{r'} + g_{\alpha}^{z'})/2$. If groups or other clusters exist behind the cluster, this model would fail to incorporate those effects. Since this would bias the mass measurement of the main cluster, this is considered separately in Sections 3.4.1 and 5. The LSS lensing model allows us to statistically estimate the lensing signals of *real* background structure from the observing data and the LSS bias in the mass measurement. We thus use the LSS lensing model for the main analysis of this paper.

We also conduct the cluster and subhalo mass measurements taking into account the error covariance matrix of uncorrelated large-scale structure along the line-of-sight, (e.g., Schneider et al. 1998; Hoekstra 2003; Umetsu et al. 2011; Oguri et al. 2010; Oguri & Takada 2011; Okabe et al. 2013), instead of the above LSS lensing model. The LSS error covariance matrix is estimated from the weak-lensing power spectrum (e.g., Schneider et al. 1998; Hoekstra 2003) with *WMAP7* cosmology (Komatsu et al. 2011). Since we fully take into account both the LSS error matrix and the statistical noise caused by the intrinsic shapes of the galaxies and the noise in the shape measurement, this approach is complementary to the LSS lensing model.

Table 2
Known Background Systems Appearing in the Mass Maps

ID ^a	Name	z_{phot}^b	Reference
A	MaxBCG J195.08820+26.78870	0.162	Koester et al. (2007)
B	GMBCG J195.47315+26.95810	0.219	Hao et al. (2010)
C	MaxBCG J195.47907+27.16429	0.208	Koester et al. (2007)
D	GMBCG J195.34791+29.07201	0.189	Hao et al. (2010)
E	MaxBCG J195.34617+29.18616	0.170	Koester et al. (2007)
F	NSC J125939+290715	0.189	Gal et al. (2003)
G	GMBCG J193.96542+28.51557	0.257	Hao et al. (2010)
H	MaxBCG J193.92901+28.76123	0.259	Koester et al. (2007)
I	SDSSCGB 06685	0.183	McConnachie et al. (2009)
J	WHL J125535.3+273104	0.418	Wen et al. (2009)

Notes.

^a The identification of background systems in Figure 3.

^b Photometric redshifts.

However, the statistical error is dominated in subhalo mass measurements (see Section 3.4.2), and it is difficult to identify *real* background structure using the error matrix.

3. WEAK-LENSING ANALYSIS FOR SUBHALOS

3.1. Projected Distributions of Mass and Baryons

We first make maps of the lensing convergence field ($\kappa(\boldsymbol{\theta})$), luminosity ($l(\boldsymbol{\theta})$) and number density ($n(\boldsymbol{\theta})$) of member galaxies and the model of the LSS lensing signal ($\kappa_{\text{LSS}}(\boldsymbol{\theta})$). In order to identify subhalos in a model independent way, the projected mass distribution is reconstructed following Kaiser & Squires (1993) with a Gaussian smoothing kernel. The details of map-making are explained in Appendix B. We adopt various smoothing scales in the range of $r_{\text{sm}} = 1, \dots, 5$ arcmin, stepped by 0.1 for 1–2 arcmin and 0.2 for 2–5 arcmin, to optimize the detection of subhalos with various mass properties. The definitions of subhalos are described in the next subsection. We present here the correlation between mass and luminous matter on the projected distribution.

Figure 3 shows the significance map, ν , defined by κ/σ_{κ} , with a smoothing scale of FWHM = 4' ($r_{\text{sm}} = 2.4$), where the reconstruction error, σ_{κ} , is calculated over local background galaxies (see Appendix B) where a typical value in this smoothing scale is $\sigma_{\kappa} \simeq 7.7 \times 10^{-3}$. The LSS lensing model was not taken into account. The mass distribution in the central region, in which two cD galaxies NGC 4874 (α, δ) = (194°898, 27°959) and NGC 4889 (195°034, 27°977) exist, is elongated in the east and west directions. Clumpy structures are found everywhere, but anisotropically distributed. In particular, the projected distribution of clumpy structures is concentrated 30–60' south-west of NGC 4874. Some clumpy structures are associated with background groups in the literature (letters in Figure 3 and Table 2).

The left and middle panels of Figure 4 show maps of luminosity and the number density of member galaxies, overlaid with the contours of the projected mass distribution. The mass and galaxy distribution are clearly correlated with each other. The right panel of Figure 4 is the convergence map of the LSS lensing model. The S/Ns of the LSS lensing map are at most 0.4σ , and thus, the LSS lensing effect accounts for a small fraction of the observed signal. However, the LSS model fails to describe the lensing signals around some groups behind the cluster (Table 2). The reason is likely that the estimation of the LSS lensing effect is based on galaxy–galaxy lensing which

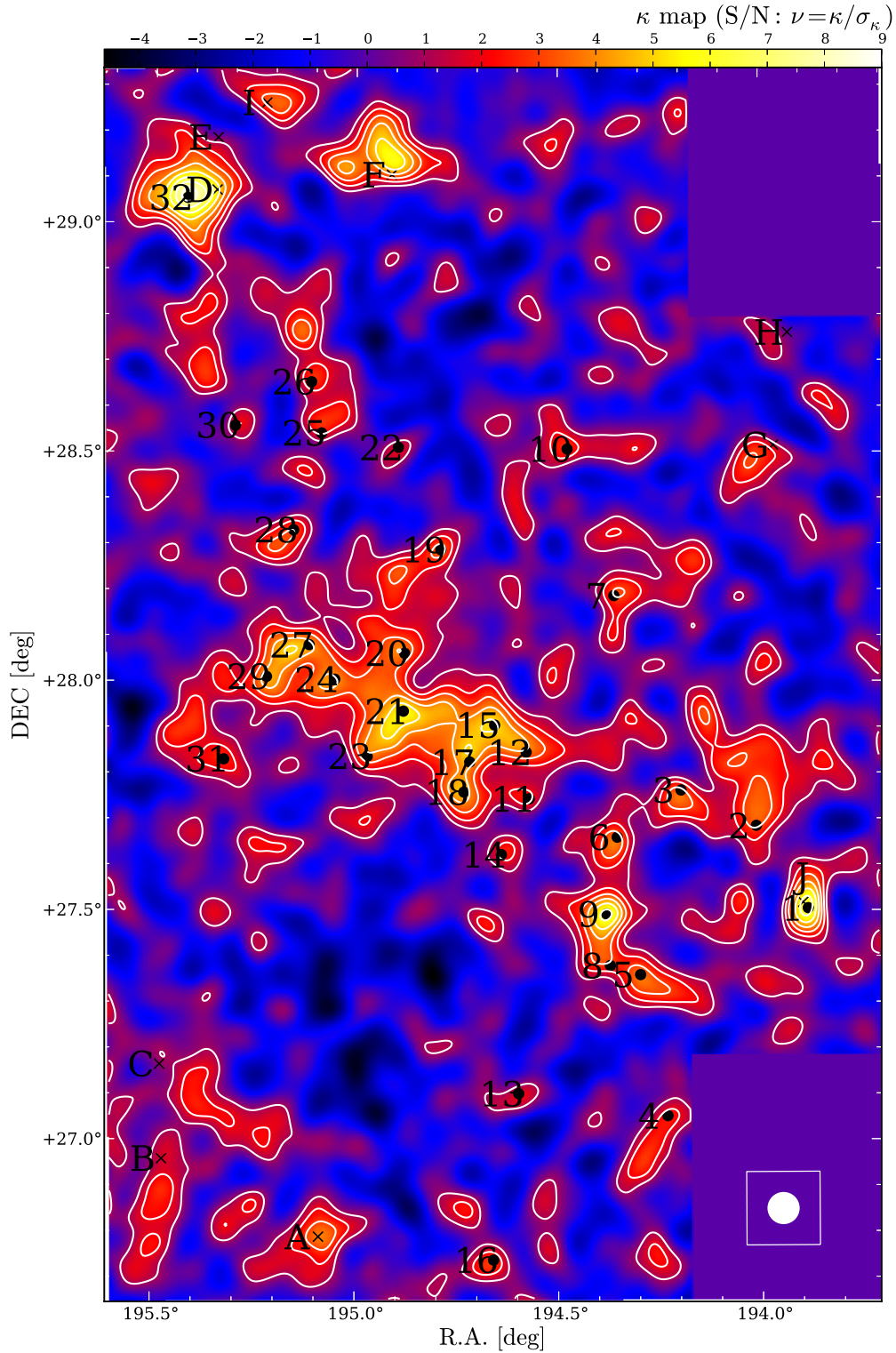


Figure 3. Projected mass distribution with a smoothing scale of FWHM = $4'$ and units of significance of $\nu = \kappa/\sigma_\kappa$. The shear is used without taking into account the LSS lensing effect. The contours of significance start at 1σ with a step value of 1σ . The letters and numbers denote the names of known background systems (Table 2) and the names of subhalos (Table 3), respectively.

(A color version of this figure is available in the online journal.)

fails to take group-scale or cluster-scale structures into account. This is further elaborated in the Section 3.4.1.

To quantify the correlations shown in the maps, we compute the pixel-to-pixel coefficients between the mass maps ($\kappa(\theta)$) and the luminosity ($l(\theta)$) and density ($n(\theta)$) maps for member galaxies. The resultant coefficients for both $\langle \kappa l \rangle$ and $\langle \kappa n \rangle$ change

from 0.57 ± 0.08 (7σ) to 0.16 ± 0.02 (8σ) with a decrease in spatial resolution. Here, the errors are estimated by bootstrap re-sampling with 200 realizations of κ maps, describing that noise peaks are accidentally correlated with smoothed luminous distributions. In short, the correlation between mass and member galaxy distributions is at the level of 7σ – 8σ . We also computed

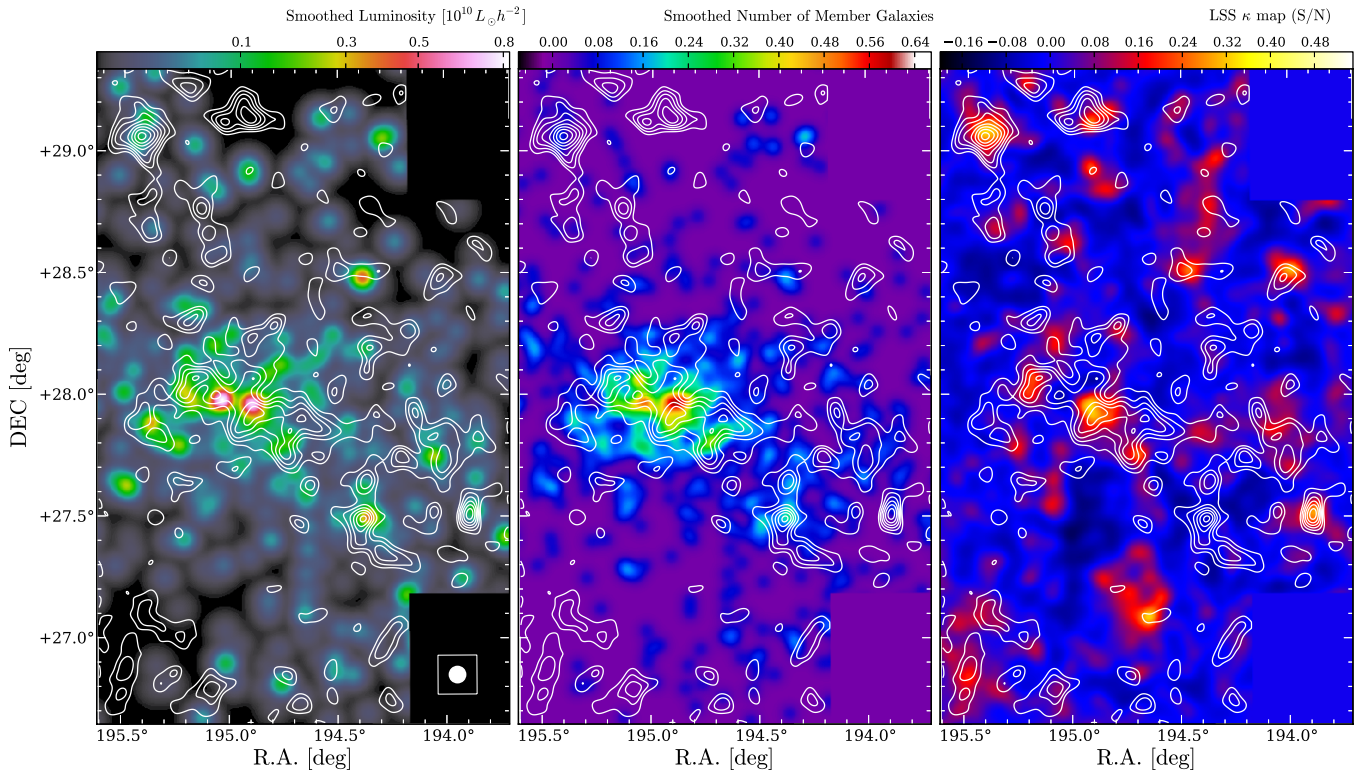


Figure 4. Luminosity map for member galaxies spectroscopically identified in the SDSS DR8 and NED catalog ($i' < 18$; Section 2.5). The contours of the lensing κ -field are overlaid in units of 1σ reconstruction error (Figure 3), without taking the LSS lensing model into account. Middle: density map for member galaxies. Right: mass map of the LSS lensing model estimated from galaxy–galaxy lensing using photometric redshifts and luminosities for individual galaxies (Section 2.6). (A color version of this figure is available in the online journal.)

the coefficients between the mass map and the LSS lensing map ($\kappa_{\text{LSS}}(\theta)$), and found high correlation, 0.51 ± 0.08 (6σ) for $r_{\text{sm}} = 5'$ and 0.28 ± 0.02 (14σ) for $r_{\text{sm}} = 1'$, respectively. The significance level is higher with an increase in resolution, indicating that the LSS lensing signal caused by small background objects creates a local shear pattern.

As shown in Figure 5, the X-ray surface brightness distribution of *ROSAT* X-ray satellite shows an elongated X-ray distribution in the central region and an excess X-ray flux associated with the NGC 4839 group in the southwest direction (Briel et al. 1992; White et al. 1993; Neumann et al. 2001). Mass contours are overlaid with a smoothing scale of $\text{FWHM} = 8'.33$ to compare with the diffuse emission detected with a large PSF of the *ROSAT*. Although the diffuse X-ray emission from the NGC 4839 group is associated with a clumpy mass structure, all mass structures are not necessarily correlated with X-ray features. This point is further discussed in Section 6.6.

3.2. Selection and Mass Measurements of Subhalos

We explore, in a model-independent way, subhalo candidates by finding peaks in the mass maps reconstructed using several smoothing scales. As described in Section 3.1, maps of the observed lensing signals are correlated with those of the LSS lensing model (Figure 4). In order to securely identify cluster subhalos and accurately measure their masses, it is crucial to minimize the contamination by the LSS lensing effect. We therefore calibrate the reduced shear with an approximate form of $g_{\alpha}^{(\text{corr})} = g_{\alpha} - g_{\alpha}^{\text{LSS}}$ to eliminate the LSS lensing effect along the line-of-sight as much as possible. Mass reconstructions are then repeated using the calibrated shear catalog.

Subhalo candidates with peaks above a threshold in the mass maps are selected. The mass maps are represented as the convolution of the lensing distortion pattern of a cluster mass distribution with smoothing kernels. Therefore, the Gaussian smoothing scales used for the mass reconstruction vary from $1'$ to $5'$ in order to optimize for the detection of subhalos with various mass properties. Here, the pixelized κ field changes slightly using the reconstruction kernels, similar to top-hat or wavelet filters.

We use a significance level, $\nu \equiv \kappa/\sigma_{\kappa}$, for the selection of subhalo candidates, where κ and σ_{κ} are the dimensionless surface mass density and the reconstruction error, respectively. Since the variance and skewness of the ν histogram in the pixels depend on the smoothing scale, we identify subhalo candidates above a threshold set at three times the standard deviation. The threshold of significance in the highest resolution corresponds to $\nu > 3.4$. We first identify subhalo candidates at various smoothing scales. Then, two peaks appearing between two different smoothing scales are matched with the condition $d < \text{FWHM}$, where d is the distance between the two peaks which appeared in different scales, and FWHM is the full width and half the maximum of the larger smoothing scale. This process results in 49 subhalo candidates. We note that Okabe et al. (2010a) used a mass map with single smoothing scale ($\text{FWHM} = 2'$) and applied the lower threshold. Therefore, two of the seven subhalo candidates in the previous paper (Okabe et al. 2010a; numbers 6 and 8) are below a more conservative threshold of this analysis.

Since we minimized the LSS lensing contribution by applying the galaxy–galaxy lensing model, eight known background objects (Table 2) are below the thresholds selected. However,

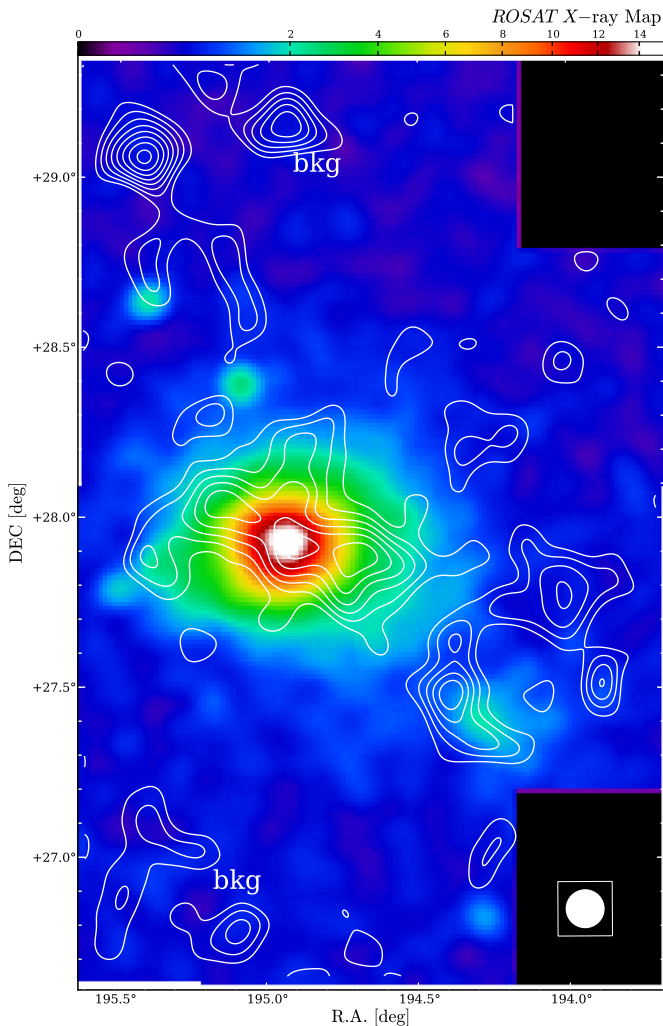


Figure 5. X-ray surface brightness distribution in the 0.1–2.4 keV band from ROSAT X-ray satellite. The contours of the mass map are overlaid with $\text{FWHM} = 8.3$, taking into account the LSS lensing model. The contour level starts at 1σ and increases in steps of 1σ .

(A color version of this figure is available in the online journal.)

the model does not perfectly describe the full LSS lensing effect. Three other peaks associated with the known background objects (Table 2) are detected with the above conditions. One is the background object “I” and two peaks are around the object “F” (see Figure 3). These objects are likely to be groups because the lensing signals are stronger than what is expected from the luminosity of a single galaxy. Furthermore, there is a possibility that background groups are accidentally superimposed with cluster subhalos, giving a systematic bias on mass estimates of subhalos. This point is discussed in Section 3.4.1.

Next, we measure the model-independent projected masses (Clowe et al. 2000, see also Appendix C) for shear-selected subhalo candidates. This measurement has several important advantages. First, a large number of background galaxies are available, because a projected mass within a circular aperture radius is computed by integrating source galaxies outside the radius. The measured projected mass is a cumulative function of radius. Thus, this approach suppresses the random noise relevant to the intrinsic ellipticity, compared to a tangential distortion profile, which averages the tangential component of all background galaxies residing in radial bins. Second, since the measurement subtracts the background mass density

surrounding subhalos, the contribution of the main cluster mass distribution to subhalo masses is excluded. Third, the mass density of subhalos is expected to be close to zero outside of the tidal radius, and the measured aperture mass corresponds to the subhalo mass itself. If the mass density profile follows the universal NFW profile (Navarro et al. 1996, 1997) without any truncation radii, the aperture mass is higher than the spherical one (Okabe et al. 2010b). As expected from tidal destruction, the radial profile of the projected mass is saturated outside the truncation radii, r_t . We measure projected masses for all the candidates. Since the smoothing kernel for the mass reconstructions gives rise to centroid uncertainties of the candidates, we determine the central position by choosing maximal lensing signals within a $8' \times 8'$ box where the center is aligned with the map peak position. For accurate mass measurements of subhalos with a variety of sizes, it is important to explore truncation radii where the projected mass profile is saturated. We systematically compute projected mass profiles by changing the background annulus and then statistically determining the truncation radii. Here, the inner radius changes from 0.7 to 14.5 in steps of 0.2 and the width is fixed at $3'$. The projected mass M_{2D} is computed from saturated values, taking into account the error covariance matrix. The measurement method is detailed in Appendix C. The same analysis was repeated for different background widths which showed that the result does not significantly change. Mass measurements used a considerably large number of source galaxies ($4 \times 10^3 - 2 \times 10^4$). The number is comparable or less than that for main clusters at $z \sim 0.2$ (e.g., Okabe et al. 2010b) for which the background number densities are $n_g \sim 5 - 20$ (arcmin $^{-2}$). Less massive subhalos which are detected inside more massive ones should be excluded in order to avoid double-counting these subhalos. We count the i th subhalo using two conditions of the radius $r_{t,i} > r_{t,j}$ and the subhalo mass $M_{2D,i} > M_{2D,j}$ ($i \neq j$). The number of candidates is then reduced from 49 to 39 using this procedure. As mentioned above, the LSS model fails to fully explain the lensing signals of background systems, especially on group scales. Furthermore, since there is a possibility to detect mass structures behind the cluster, we conservatively select the candidates hosting spectroscopically identified member galaxies within their truncation radii as the cluster subhalos. Having applied these limitations, 32 peaks are identified as dark matter subhalos. Three candidates are associated with the background systems (Table 2). Four candidates have no optical counter: they are located around $\sim 70'$ in the south-east direction and the north-west direction, respectively.

These 32 subhalos are labeled by integers, in the order of right ascension. The resulting subhalo masses, M_{2D} , range from $\sim 2 \times 10^{12} h^{-1} M_\odot$ to $\sim 5 \times 10^{13} h^{-1} M_\odot$ (Table 3). As shown in Figure 6, the radial profiles of the projected mass clearly show saturation at some outer radii. The subhalos are widely distributed from the northeast to the southwest in the sky (Figure 3). Interestingly, the direction connecting between the Coma cluster and A1367 which are parts of the Coma supercluster (Gregory & Thompson 1978) agrees roughly with the subhalo distributions. Several massive subhalos are associated with well-known, spectroscopically identified groups in the cluster (e.g., Mellier et al. 1988; Adami et al. 2005). Galaxies or groups associated with subhalos are summarized with references in Table 3. The cD galaxies, NGC 4874 and NGC 4889, are associated with subhalos “21” and “24,” respectively. The mean mass ratio reported in this paper compared to the previous paper for overlapping subhalos is $\langle M_{\text{new}}/M_{\text{old}} \rangle = 1.02 \pm 0.54$.

Table 3
The Properties of Subhalos

ID ^a	(R.A., Decl.) ^b (deg)	M_{2D} ^c ($10^{12} h^{-1} M_{\odot}$)	ν ^d	Representative Galaxies ^e
1 ^f	(193.885, 27.505)	15.42 ± 2.79	5.98	NGC 4807
2	(194.011, 27.685)	8.79 ± 4.69	3.55	NGC 4816 Group ^h
3	(194.197, 27.763)	3.71 ± 1.08	4.61	SDSS J125645.42+274638.0
4	(194.232, 27.053)	2.89 ± 1.08	3.51	SDSS J125647.00+270324.9
5	(194.298, 27.360)	5.00 ± 2.34	3.86	2MASX J12571076+2724177
6	(194.355, 27.660)	2.52 ± 1.27	4.45	G12 Group ^k
7	(194.361, 28.187)	5.99 ± 2.84	3.80	UGC08071, 2MASX J12572841+2810348
8	(194.372, 27.380)	1.87 ± 0.73	3.54	2MASX J12573148+2723048
9	(194.381, 27.493)	12.11 ± 2.52	6.45	NGC 4839 Group ^h , G4 Group ⁱ , NGC 4842, X-ray subhalo ^m
10	(194.477, 28.507)	3.24 ± 0.75	3.42	2MASX J12575392+2829594
11	(194.572, 27.745)	4.13 ± 0.85	4.03	2MASX J12581922+274543
12	(194.579, 27.846)	2.02 ± 0.78	3.87	SDSS J125818.20+275054.5
13	(194.597, 27.101)	2.70 ± 0.77	3.61	2MASX J12581552+2705137
14	(194.640, 27.623)	4.51 ± 1.27	3.53	NGC 4853
15	(194.656, 27.905)	2.96 ± 1.44	6.90	NGC 4839 Group ^h
16	(194.659, 26.738)	5.03 ± 1.06	4.19	SDSS J125839.93+264534.2
17	(194.718, 27.825)	3.13 ± 0.74	4.94	G9 Group ⁱ , SA 1656-030 ^j
18	(194.732, 27.759)	6.48 ± 2.03	4.47	G8 Group ⁱ
19	(194.790, 28.288)	4.66 ± 1.26	4.74	SDSS J125914.99+281503.6
20	(194.879, 28.062)	2.90 ± 1.58	4.16	2MASX J12593141+2802478
21	(194.882, 27.936)	4.29 ± 1.06	7.23	NGC 4874(cD), part of G1 Group ⁱ , X-ray subhalo 2 ^l
22	(194.895, 28.511)	4.50 ± 1.90	3.54	2MASX J12594129+2830257
23	(194.971, 27.837)	3.75 ± 1.04	4.26	J194.9353+27.83393 ^k , SA 1656-054 ^l , X-ray subhalo 3 ^l
24	(195.052, 28.005)	5.20 ± 2.40	4.71	NGC 4889(cD), part of G1 Group ⁱ X-ray subhalo 1 ^l
25	(195.086, 28.542)	3.86 ± 0.95	3.93	2MASX J13002268+2834285
26	(195.111, 28.654)	2.75 ± 0.79	4.43	SDSS J130037.14+283950.9
27	(195.115, 28.080)	4.28 ± 1.74	6.24	SDSS J130030.95+280630.2, part of G7 Group ⁱ
28	(195.155, 28.331)	5.70 ± 1.68	3.68	NGC 4896
29	(195.220, 28.010)	3.64 ± 1.30	4.31	NGC 4908, NGC 4908 Group
30	(195.300, 28.558)	3.12 ± 0.66	4.03	SDSS J130114.96+283118.3
31	(195.325, 27.830)	2.97 ± 1.42	3.41	G4 Group ⁱ , NGC 4919
32 ^g	(195.421, 29.054)	45.95 ± 7.57	8.35	G15 Group ⁱ , IC 4088, 2MASX J13014399+2859587

Notes.

^a Subhalo name.

^b Weak-lensing center in units of deg.

^c Subhalo mass in units of $10^{12} h^{-1} M_{\odot}$.

^d Maximum signal-to-noise ratio appearing in the mass maps (κ).

^e Name of representative galaxies or optical groups.

^f Possibly an overlapped background structure, WHL J125535.3+273104 (Table 2).

^g Possibly an overlapped background structure, GMBCG J195.34791+29.07201 (Table 2).

^h Mellier et al. (1988).

ⁱ Adami et al. (2005).

^j Conselice & Gallagher (1999).

^k Adami et al. (2009).

^l Andrade-Santos et al. (2013).

^m Briel et al. (1992).

We also measured the projected masses for two subhalos with peaks below the threshold in this analysis. The mean mass ratio is $\langle M_{\text{new}}/M_{\text{old}} \rangle = 0.74 \pm 0.66$. Since the number density of background galaxies in the previous analysis is about half of that reported in this analysis, we cannot rule out the possibility that these peaks are actually above the threshold.

3.3. Stacked Lensing Analysis for Subhalos

Next, we conducted a stacked lensing analysis for the subhalo candidates, which is complementary to the projected mass measurement. The power of the stacked lensing technique is to reduce the random noise due to intrinsic ellipticities by increasing the number of source galaxies. Tangential profiles, even for small and less massive subhalos, can be computed

and their average parameters can be determined with lower measurement errors.

We first divide the subhalos into three subsamples based on the model-independent projected masses of $M_{2D} \leq 4.6 \times 10^{12} \times 10^{12} h^{-1} M_{\odot}$, $4.6 \times 10^{12} h^{-1} M_{\odot} \leq M_{2D} \leq 10^{13} h^{-1} M_{\odot}$ and $10^{13} h^{-1} M_{\odot} \leq M_{2D}$. The mass thresholds are chosen by a subhalo mass function which is described in Section 6.1. The number of subhalos are 21, 8, and 3, progressing from less massive to more massive subhalos. Figure 7 shows that the tangential component is positive (top panel), and the 45° rotated component is positive and negative in random order (bottom panel). The mean of the 45° rotated component over the radial range is consistent with a null signal, within the error of the mean. A sharply truncated feature is found in the

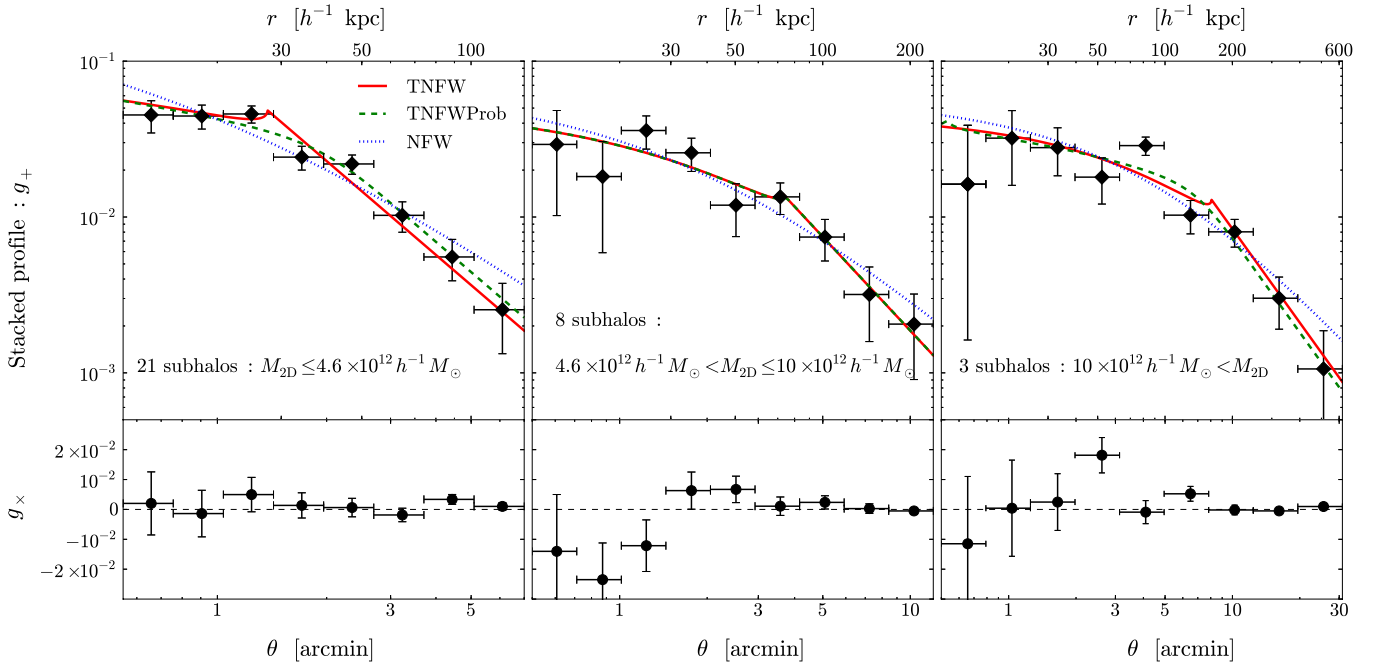


Figure 7. Mean distortion profiles obtained by azimuthally averaging the measured galaxy ellipticities for 32 subhalos. The subsamples are selected with model-independent projected masses. Left: 21 subhalos with $M_{2D} \leq 4.6 \times 10^{12} h^{-1} M_{\odot}$. Middle: 8 subhalos with $4.6 \times 10^{12} h^{-1} M_{\odot} < M_{2D} \leq 4.6 \times 10^{12} h^{-1} M_{\odot}$. Right: 3 subhalos with $10 \times 10^{12} h^{-1} M_{\odot} < M_{2D}$. The profile slopes drastically change at the truncation radii. The red solid, green dashed, and blue dotted curves are the best-fit TNFW, TNFWProb, and NFW models, respectively. The NFW and TNFWProb models adequately describe a sharp truncation, while the NFW model for less massive (left) and massive (right) subsamples is strongly disfavored. The best-fit truncation radius increases with an increasing mass of the subsample.

(A color version of this figure is available in the online journal.)

Table 4
Best-fit Mass Parameters for TNFW and TNFWProb Models for Lensing-selected Subhalos

Sub-sample ^a	N_{sub}^b	M_{sub}^c ($10^{12} h^{-1} M_{\odot}$)	r_t^c ($h^{-1} \text{kpc}$)	$\langle M_{\text{sub}} \rangle^d$ ($10^{12} h^{-1} M_{\odot}$)	$\langle r_t \rangle^d$ ($h^{-1} \text{kpc}$)	$\sigma_{r_t}^d$ ($h^{-1} \text{kpc}$)	$\langle L_i' \rangle^e$ ($10^{10} h^{-2} L_{i', \odot}$)	S/N ^f	$\mathcal{P}_{\text{fake}}^g$
$< 4.6 \times 10^{12} h^{-1} M_{\odot}^h$	21	$2.91^{+0.28}_{-0.29}$	$27.48^{+2.43}_{-1.91}$	$3.53^{+0.49}_{-0.44}$	$35.57^{+4.78}_{-4.53}$	$9.97^{+5.41}_{-4.38}$	2.11	13.69	0.019
$(4.6-10) \times 10^{12} h^{-1} M_{\odot}$	8	$5.93^{+1.43}_{-1.11}$	$72.79^{+25.42}_{-15.07}$	$5.95^{+1.66}_{-1.12}$	$73.18^{+33.06}_{-12.20}$	< 1.75	5.24	8.67	0.011
$10^{13} h^{-1} M_{\odot}^h$	3	$26.72^{+4.28}_{-4.10-5.88}$	$161.15^{+57.25}_{-22.33}$	$23.13^{+7.37}_{-6.33-5.06}$	$127.11^{+71.86}_{-35.22}$	$33.31^{+18.39}_{-18.95}$	7.49	5.35	2×10^{-5}
0–20'	11	$3.05^{+0.56}_{-0.58}$	$35.10^{+5.28}_{-4.26}$	$3.05^{+1.49}_{-0.62}$	$35.66^{+23.02}_{-4.65}$	< 19.71	5.35	8.25	0.082
20'–40'	10	$5.00^{+0.74}_{-0.65}$	$49.29^{+8.76}_{-7.66}$	$5.00^{+0.73}_{-0.65}$	$49.29^{+9.77}_{-11.84}$	< 19.43	3.47	10.70	0.062
40'–60'	8	$5.43^{+1.04}_{-1.33-0.73}$	$65.08^{+10.55}_{-19.51}$	$4.84^{+1.24}_{-1.09-0.17}$	$49.56^{+13.78}_{-11.42}$	$14.62^{+9.62}_{-7.81}$	1.52	8.39	0.023
60'–80'	3	$30.29^{+3.21}_{-3.23-1.75}$	$209.69^{+2.99}_{-13.29}$	$30.27^{+5.22}_{-4.12-1.75}$	$209.31^{+4.87}_{-39.86}$	< 19.00	6.16	7.62	5×10^{-5}

Notes.

^a Name of subsamples for subhalos in the stacked lensing analysis.

^b Number of subhalos.

^c Best-fit subhalo mass and truncation radius for the TNFW model.

^d Best-fit subhalo mass, and the average and standard error of the truncation radius for the TNFWProb model.

^e Average luminosity for associated galaxies, estimated by weighting tangential distortions, g_+ .

^f Signal-to-noise ratio for the tangential distortion profile.

^g Probabilities that the TNFW mass and truncation radius represent false subhalos are within 1σ contours for the best-fit values of observed subhalos.

^h The NFW model is strongly disfavored.

is an extreme case of truncation models, where the mass density outside the truncation radius is zero as described in Appendix D. The TNFWProb model is the TNFW model taking into account a probability function for the truncation radius which is assumed to be Gaussian with the mean, $\langle r_t \rangle$, and the standard error σ_{r_t} . Given this function, we measure a mean subhalo mass $\langle M_{\text{sub}} \rangle$. In the process of fitting the model, we propagate systematic errors by possible background structures around subhalos “1” and “32,” which is described in Section 3.4.1. As expected from the clear truncation feature,

the mean tangential profiles are well fitted using the TNFW and TNFWProb models (Figure 7). The best-fit subhalo masses and truncation radii are listed in Table 4. The best-fit mass and truncation increase with increasing model-independent projected masses. If the subhalo sample was entirely from false peaks, these characteristic features could not be found. We compute the significance probability, $Q(\nu/2, \chi_{\text{min}}^2/2)$, that the data shows as a poor fit, as the observed value of χ_{min}^2 by chance. The NFW models for the lowest- and highest-mass samples are rejected with a significance level of $Q = 4\%$.

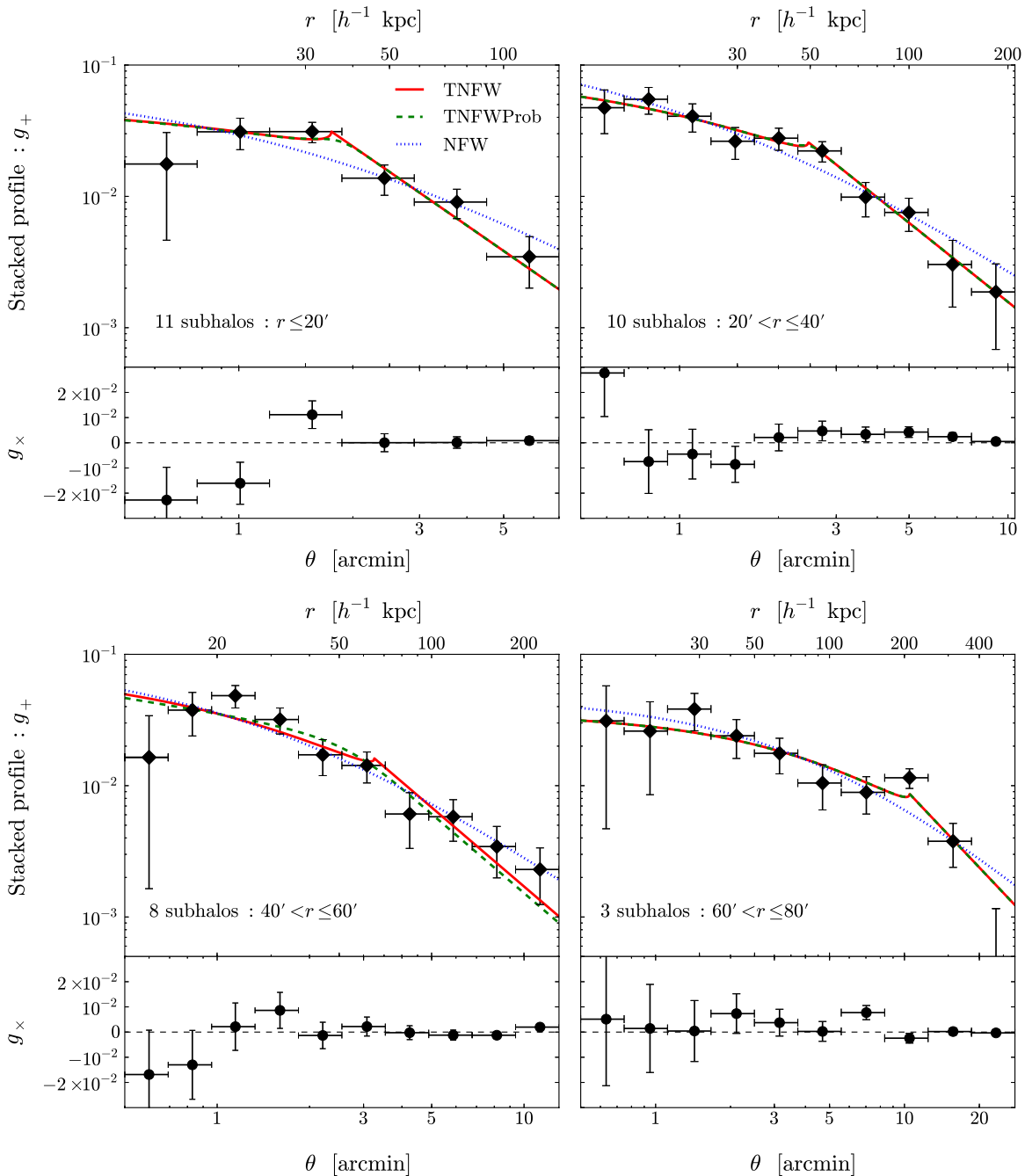


Figure 8. Mean distortion profile for four subsamples of 32 subhalos, selected by the projected cluster-centric radii of 0–20′ (top-left), 20–40′ (top-right), 20–40′ (bottom-left), and 60–80′ (bottom-right). The red solid, green dashed, and blue dotted curves are the best-fit TNFW, TNFWProb, and NFW models, respectively. (A color version of this figure is available in the online journal.)

Thus, the NFW model is inadequate to describe the tangential shear profile with breaks. The mean ratio between the best-fit subhalo masses and the mean projected mass of the subsamples, $\langle M_{2D} \rangle$, are $\langle \langle M_{2D} \rangle / M_{\text{sub}} \rangle = 1.02 \pm 0.12$ for the TNFW model and $\langle \langle M_{2D} \rangle / M_{\text{sub}} \rangle = 1.06 \pm 0.15$ for the TNFWProb model, respectively. These two models are in good agreement.

Next, we repeat the stacked lensing analysis for four subsamples divided by the projected cluster-centric radii (0–20′, 20–40′, 40–60′, and 60–80′). Since tidal destruction predicts that the truncation radii are statistically correlated with the three-dimensional radius, a stacked procedure averages out line-of-sight positions for subhalos. This provides information regarding the dependence of mean subhalo size

on the cluster-centric radius. Figure 8 displays the mean tangential profiles with clear breaks. The TNFW and TNFWProb models give a better fit to the stacked profiles (Table 4). Although the NFW model fit is acceptable ($Q > 10\%$), the TNFW and TNFWProb are preferred based on comparing the goodness-of-fit of each model. The mean truncation radius increases as the projected radius from the cluster center increases. The mean mass ratios are $\langle \langle M_{2D} \rangle / M_{\text{sub}} \rangle = 0.97 \pm 0.11$, and $\langle \langle M_{2D} \rangle / M_{\text{sub}} \rangle = 1.00 \pm 0.16$ for the TNFW and TNFWProb models, respectively.

Previous papers (e.g., Natarajan et al. 2007, 2009; Limousin et al. 2005, 2007) estimated subhalo masses by galaxy–galaxy lensing method using a model of a pseudo-isothermal elliptical

mass distribution (PIEMD) of which three-dimensional mass density is given by $\rho \propto (1 + r^2/r_{\text{core}}^2)^{-1}(1 + r^2/r_{\text{cut}}^2)^{-1}$. Here, the core radius r_{core} is at the order of 100 pc (Limousin et al. 2005) and r_{cut} is the truncation radius. The tangential shear for the PIEMD model (Natarajan et al. 2007) falls as $\gamma_t \propto r^{-1}$ in the transition region ($r_{\text{core}} < r < r_{\text{cut}}$) and $\gamma_t \propto r^{-2}$ in the outer region ($r_{\text{cut}} < r$). We also tried to fit the stacked lensing signals with the PIEMD model. Here we assume that the core radius is one-hundredth of the truncation radius, because there is no data on scales of sub kpc and thus we cannot constrain it. We also assume a spherical model for the simplicity. The PIEMD model gave a poor fit because the slope of the model in the transition region ($r_{\text{core}} < r < r_{\text{cut}}$) is different from the observed profile for the mass scales of our subhalos.

3.4. Systematic Errors

In this section, we assess various systematic errors on the subhalo analysis, such as a projection effect on subhalo mass measurements (Section 3.4.1), LSS error covariance matrix (Section 3.4.2), a probability of spurious peaks (Section 3.4.3), selection criteria of subhalos (Section 3.4.4) and stacking procedure (Section 3.4.5). They are critically important for further discussion of subhalo properties such as a mass function (Section 6.1; construction of Figure 13). Each systematic error would have an independent effect on the mass function. For instance, the projection effect would lead to a bias in subhalo mass measurements (the x -axis of the mass function). A contamination of spurious peaks and selection criteria would change a shape of the mass function (the y -axis), especially on small mass scales.

3.4.1. Projection Effect

The projection effect on lensing mass measurement of cluster subhalos, caused by background groups accidentally superimposed along the line-of-sight, is examined here. Although LSS modeling is quantified based on scaling relations between mass and luminosities, it fails to fully describe massive background structures, such as groups or clusters. This effect would lead to a bias in mass estimates, possibly changing the mass of the x -axis in the mass function (Section 6.1; Figure 13). As shown in Figure 3, possible background structures, J and D (Table 2), are located within two subhalo regions labeled “1” and “32” (Table 3), respectively. Although it is in principle very difficult to discriminate between them from the observed lensing signal, a difference between the expected mass density profiles enables us to assess a contribution from background structures in the observed lensing signal. Since interior subhalos are tidally destroyed by their parent halos, it is expected that the mass density profile outside the tidal radius sharply declines. On the other hand, virialized background groups or clusters do not show such a feature as long as there is no neighboring massive halo. Indeed, tangential distortion profiles for individual groups or clusters and stacked profiles show a clear curvature as a characteristic signature of the NFW prediction and no evidence of a truncation feature (e.g., Johnston et al. 2007; Okabe et al. 2010b, 2013; Umetsu et al. 2011; Oguri et al. 2012; Taylor et al. 2012). Thus, fitting models to tangential distortion profiles helps us to discriminate between subhalos and background objects. As mentioned above, the profile for less massive subhalos is very noisy and slightly changed by the choice of radial bins, because the number of source galaxies is small in proportion to the area surrounding less massive subhalos. We therefore concentrate on

Table 5
Best-fit Masses and Truncation Radii for Three Massive Subhalos Using the Tangential Distortion Profiles

ID ^a	M_t^b ($10^{12} h^{-1} M_\odot$)	r_t^c (h^{-1} kpc)	$\chi_{\text{min}}^2/\text{d.o.f}^d$	S/N ^e	$\chi_{\text{min}}^2/\text{d.o.f}$ (NFW) ^f
1	14.26 ^{+2.37} _{-2.53-5.55}	77.22 ^{+2.74} _{-3.81}	5.38/3	6.17	8.79/4
9	11.05 ^{+1.83} _{-1.84}	68.70 ^{+5.54} _{-9.49}	0.59/3	5.99	1.97/4
32	47.65 ^{+5.81} _{-5.81-13.42}	184.38 ^{+14.75} _{-16.65}	3.74/5	8.33	11.31/6

Notes.

^a Name of subhalos (Table 3).

^b Best-fit mass, in units of $10^{12} h^{-1} M_\odot$.

^c Best-fit truncation radii, in units of h^{-1} kpc.

^d Reduced chi-square for the best-fit truncated NFW (TNFW) model (d.o.f is the degrees of freedom).

^e Signal-to-noise ratio for the tangential distortion profile.

^f Reduced chi-square for the best-fit NFW model. All are higher than those of the TNFW model. In particular, the significance probability, Q , for the NFW model of subhalo “32” is less than 10%, indicating that the profile is not well fitted by the NFW model.

computing distortion profiles for three massive subhalos (“1,” “9,” and “32”), with masses greater than $10^{13} h^{-1} M_\odot$.

Figure 9 displays breaks in the tangential shear profiles. The slope follows $\propto \theta^{-2}$ outside the break, as shown by stacked lensing analysis (Section 3.3). The off-centering effect (Yang et al. 2006) of the main cluster mass on the lensing signal is negligible because of large separation from the cluster center. We first fit the TNFW model as a model of subhalos to the tangential distortion profiles. We also tried to fit a truncated singular isothermal sphere (Okabe et al. 2010a) model to the profile but found a poor fit for massive subhalos. The best-fit masses and truncation radii are shown in Table 5. We found that the best-fit values do not change significantly by a choice of radial bins. The solid lines for the best-fit values describe the profiles with the breaks (Figure 9) well. Next we fit the NFW model to the data and then obtain larger minimum reduced χ_{min}^2 values than those for the TNFW model. The significance probabilities, Q , for the NFW model are 0.12, 0.74, and 0.08 for subhalos “1,” “9,” and “32,” respectively. When we adopt the threshold of 10%, the NFW model for subhalo “32” is unacceptable and for subhalos “1” and “9” are acceptable although Q for subhalo “1” is close to the threshold. If observed lensing signals around subhalos “1” and “32” were explained only by background objects, the profiles should be well described by the NFW model. We repeat the tangential fits using photometric redshifts $z_{\text{phot}} = 0.418$ and 0.189 as redshifts of background objects around subhalos “1” and “32,” and obtain the virial masses for the NFW model, $M_{\text{vir}}^{(1)} = 12.11_{-4.93}^{+11.06} \times 10^{14} h^{-1} M_\odot$, and $M_{\text{vir}}^{(32)} = 3.98_{-0.91}^{+1.06} \times 10^{14} h^{-1} M_\odot$, respectively. In this mass scale, no clear truncation radius was found in the tangential profiles (e.g., Okabe et al. 2010b; Oguri et al. 2012). Thus, it implies that all lensing signals cannot be explained solely by background objects. We then fit using a combined model of the TNFW for subhalos and NFW for backgrounds, where we assume the mass and concentration relation for backgrounds (Duffy et al. 2008) and fix the truncation radius derived by fitting the TNFW model. Although measurement errors of subhalo masses become larger, we find that the best-fit subhalo masses are decreased by 30%–40%. We therefore add these differences to the second error in Table 5, as the systematic error, and propagate them into the stacked lensing analysis (Section 3.3; Table 4).

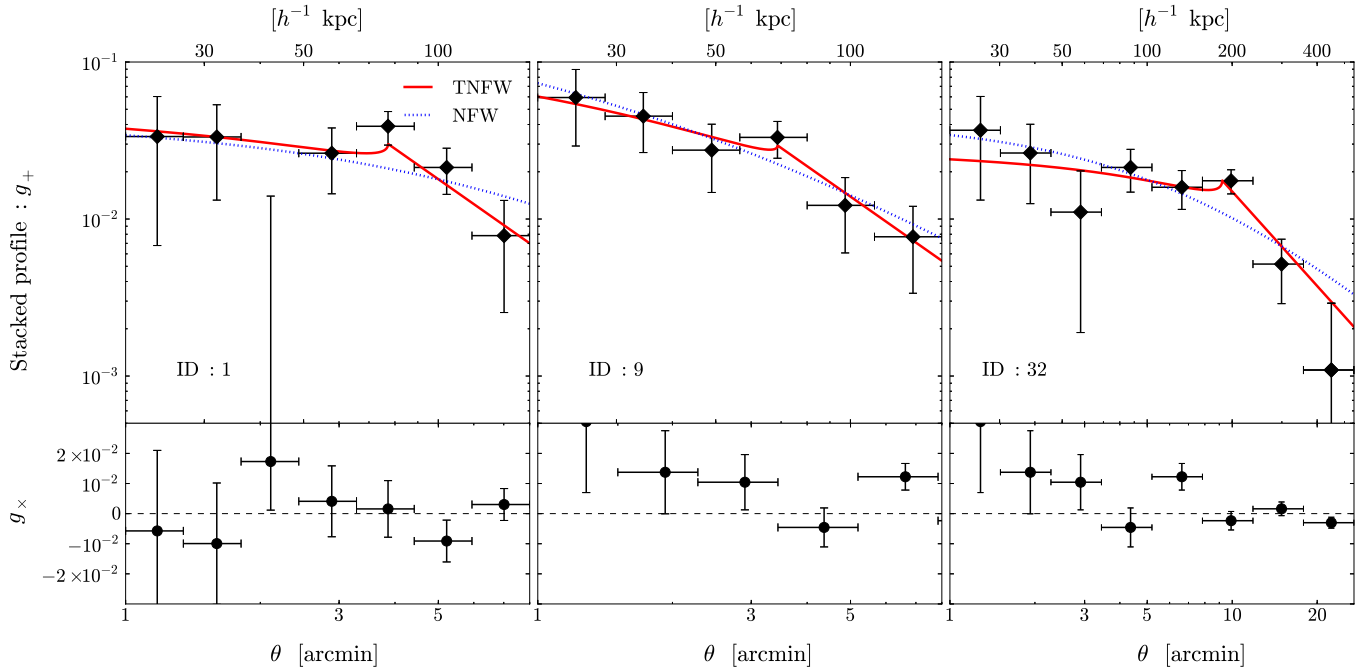


Figure 9. Radial profiles of the tangential shear component (top panel), g_+ , and the 45° rotated component (bottom panel), g_x , for three massive subhalos (“1,” “9,” and “32”; from left to right). The tangential signals sharply decline outside the truncation radii. The red solid and blue dotted lines are the best-fit for TNFW and NFW models, respectively.

(A color version of this figure is available in the online journal.)

3.4.2. LSS Error Covariance Matrix

An alternative approach to take into account LSS lensing effect in weak-lensing mass measurements is to use the error covariance matrix of uncorrelated large-scale structure along the line-of-sight (e.g., Schneider et al. 1998; Hoekstra 2003), instead of the LSS lensing model. Here we estimate the error covariance matrix $C_{ij} = C_{g,ij} + C_{LSS,ij}$ in the i - and j -th radial bin, where $C_{g,ij} = \sigma_g^2 \delta_{ij}$ is a diagonal matrix of the uncertainty caused by the intrinsic shapes of the galaxies and the noise in the shape measurement, and $C_{LSS,ij}$ is calculated by the weak-lensing power spectrum (e.g., Schneider et al. 1998; Hoekstra 2003) with *WMAP7* cosmology (Komatsu et al. 2011). The diagonal component of LSS error covariance matrix, $\sigma_{LSS} = C_{LSS}^{1/2}$, is lower than the statistical error σ_g for $r \lesssim 50'$ and comparable to those for $r \gtrsim 50'$, respectively. Thus, the statistical error is dominated in the radial range of the subhalo mass measurements. We computed the stacked tangential shear profiles from the shear catalog without LSS lensing model. As the truncation position in the tangential shear profiles does not change significantly, the best-fit truncation radii agree within 2% with those in Table 4. As the lensing signals at the truncation radii become higher than those estimated from the shear catalog with the LSS lensing, the subhalo masses for mass and radial bins become $\sim 10\%$ and $\sim 13\%$ higher. In other words, our LSS model corrects the LSS lensing bias by $\sim 10\%$. The measurement uncertainties of the subhalo mass and the truncation radius, estimated with the error covariance matrix, are consistent with those estimated from the statistical error, because the statistical error is dominated.

3.4.3. Probability of Spurious Peaks

To measure a reliable subhalo mass function, it is of critical importance to statistically rule out the possibility that the subhalo candidates are actually spurious peaks. The peak finding

method always suffers from the presence of spurious peaks. It is therefore of vital importance to quantify the number and properties of spurious peaks in order to confirm the purity of *real* subhalos. Especially, if our subhalo catalog included spurious peaks, a shape of a subhalo mass function (Section 6.1; Figure 13) would be changed. For this purpose, we create 200 bootstrap data-sets generated by randomly swapping reduced shear at fixed positions, repeat the map making process and then identify artificial false peaks which satisfy the same conditions except for the spectroscopic information of the galaxies. The number of spurious peaks is 5.32 ± 2.23 for each realization. Thus, we cannot completely rule out a contamination in the subhalo catalog. It is, however, difficult to quantify the purity of subhalos comparing the number of detected subhalo candidates and false peaks, because we excluded several subhalo candidates taking into account the cloud-in-cloud problem and the background groups. Stacked lensing analysis enables us to measure the mean parameters even for spurious peaks, although individual measurements of spurious peaks are very difficult due to high statistical noise. Comparing the statistical properties of spurious peaks allows us to discuss the purity of the subhalo catalog. We generated 500 bootstrap replications of stacked tangential profiles using the catalog of artificial false peaks. Here, the number of spurious peaks and radial bins are the same as those for subsamples in stacked lensing analysis of subhalos (Section 3.3). The mean mass and truncation radius for spurious peaks are estimated by fitting with the TNFW model. We found that 38%–45% of profiles for spurious peaks gives a poor fit ($Q < 10\%$) or are ill-constrained. This indicates that the profile shapes are different from those of observed subhalos. Indeed, the stacked lensing analysis for shear-selected subhalos shows that the best-fit truncation radius depends on the projected mass and the cluster-centric radius (Figures 7 and 8). If our sample consisted entirely of spurious peaks, such a clear dependence could not be found. To make a more robust

Table 6
Results of Stacked Lensing Analysis Using a Mock Shear Catalog

$N_{\text{sub}}^{\text{a}}$	$\langle M_{\text{sub}}^{\text{input}} \rangle^{\text{b}}$	$\sigma(M_{\text{sub}}^{\text{input}})^{\text{b}}$	$\langle r_t^{\text{input}} \rangle^{\text{b}}$	$\sigma(r_t^{\text{input}})^{\text{b}}$	$\left\langle \frac{M_{\text{sub}}^{\text{TNFW}}}{M_{\text{sub}}^{\text{input}}} \right\rangle^{\text{c}}$	$\left\langle \frac{r_t^{\text{TNFW}}}{r_t^{\text{input}}} \right\rangle^{\text{c}}$	$\left\langle \frac{M_{\text{sub}}^{\text{TNFWProb}}}{M_{\text{sub}}^{\text{input}}} \right\rangle^{\text{d}}$	$\left\langle \frac{r_t^{\text{TNFWProb}}}{r_t^{\text{input}}} \right\rangle^{\text{d}}$
21	3.5	1.0	35	10	1.01 ± 0.09 (0.11)	1.10 ± 0.12 (0.21)	1.03 ± 0.12 (0.15)	1.12 ± 0.18 (0.29)
8	7.0	2.0	70	20	0.92 ± 0.21 (0.21)	0.96 ± 0.36 (0.29)	1.04 ± 0.23 (0.23)	1.11 ± 0.44 (8)
3	20.0	5.0	130	40	1.02 ± 0.26 (0.21)	1.08 ± 0.49 (0.35)	1.03 ± 0.16 (0.20)	1.02 ± 0.21 (0.6)
11	3.0	1.0	35	20	0.98 ± 0.28 (0.17)	1.18 ± 0.38 (0.79)	1.02 ± 0.18 (0.22)	1.11 ± 0.40 (5)
10	5.0	1.0	50	20	0.92 ± 0.17 (0.18)	0.99 ± 0.33 (0.37)	1.01 ± 0.19 (0.21)	1.09 ± 0.35 (13)
8	5.0	1.0	50	15	0.93 ± 0.17 (0.19)	1.00 ± 0.35 (0.36)	1.02 ± 0.18 (0.22)	1.11 ± 0.41 (5)
3	30.0	5.0	200	20	1.04 ± 0.26 (0.24)	1.10 ± 0.28 (0.52)	1.04 ± 0.14 (0.15)	1.03 ± 0.11 (11)
64	1.0	0.5	60	20	0.91 ± 0.27 (0.47)	1.00 ± 0.20 (0.77)	1.18 ± 1.18 (1.00)	1.04 ± 0.75 (6)

Notes.

^a Number of simulated subhalos.

^b Mean and standard error of the mass ($10^{12} h^{-1} M_{\odot}$) and truncation radius (h^{-1} kpc) for simulated subhalos.

^c Mean ratio of outputs to inputs for the TNFW model. Errors shown are the standard deviation based on 500 realizations. The values in brackets are the mean measurement uncertainties.

^d Mean ratio of outputs to inputs for the TNFWProb model.

conclusion, we estimate the probability that the parameters for spurious peaks accidentally coincide with those for observed subhalos within 1σ uncertainty, based on Monte Carlo re-distributions of the best-fit values with the covariance matrix of the measurement errors. The false probabilities for individual subsamples in stacked lensing analysis, $\mathcal{P}_{\text{fake}}$, are from $10^{-3}\%$ to $\sim 8\%$ (Table 4). Multiplying the number of subhalos by the false probability in each sub-sample, the expected numbers of spurious subhalos are less than unity. Therefore, we conclude that our sample of subhalos has a high degree of purity.

3.4.4. Selection Criteria

A choice of the threshold in the S/N for mass maps results in one of the main systematic errors, because we cannot completely rule out the possibility that peak heights in mass maps are accidentally above or below the threshold due to reconstruction errors of finite sampling of background galaxies. Assuming Poisson fluctuations of the reconstruction noise, the S/N changes by $\delta(\text{S/N}) = \sqrt{\delta N_{\text{bkg}}/N_{\text{bkg}}} = N_{\text{bkg}}^{-1/4} \simeq 0.25$, where N_{bkg} is an effective number density in the smoothed mass map with the highest resolution. We repeated the same analysis with different thresholds. The sample numbers become 24 and 49 with higher and lower thresholds, respectively. This systematic error is taken into consideration to compute a subhalo mass function in Section 6.1.

3.4.5. Stacking Procedure

We investigate whether the stacking method gives systematic errors, because the mean tangential profile stacked over subhalos with various truncation radii would blunt the break feature. We make synthetic weak shear catalogs of subhalos using the analytic TNFW model and the intrinsic ellipticity. Here, the number of background sources is the same as that observed. The parameters of the TNFW model for individual subhalos are generated from a Gaussian distribution. The mean and standard error of subhalo masses and the truncation radii for simulated samples are shown in Table 6. We assume that the coefficient between the subhalo mass and the truncation radius is 0.7 and that the halo concentration is 1, for the sake of simplicity. We compute 500 samples in each stacked profile and fit them with the TNFW and TNFWProb models. As shown in Table 6, the mean tangential profiles are able to recover the input values. In TNFWProb model fitting, since the mean and standard error of

the truncation radii are degenerate, $\langle r_t \rangle$ are not well constrained in some cases, resulting in a large mean measurement error.

4. CLUSTER GALAXY–GALAXY LENSING ANALYSIS

Galaxy–galaxy lensing analysis for member galaxies selected solely by their luminosities provides us with complementary and important information regarding cluster subhalos, because the sample is unbiased with respect to the lensing definition of subhalos (Section 3). We use member galaxies with luminosities in the i' band larger than $10^{10} h^{-2} L_{i',\odot}$. We compute a stacked tangential distortion profile as a function of the radius from luminous member galaxies. Since the cluster field is crowded, neighboring luminous galaxies may lead to serious contamination in the stacked lensing profile, if they are not sufficiently separated. We thus need to determine the outermost radius of the profile in order to minimize lensing contamination from neighboring luminous members. We estimate the histogram of projected distances between the luminous member galaxies. The outermost radius is chosen to be $5'$ by applying a threshold that the mean number of neighboring luminous galaxies is less than unity. We compile 64 luminous member galaxies located in the projected cluster-centric radius of $10' < r < 80'$. Figure 10 shows the mean tangential profile. A sharply truncated profile is not found, in contrast to lensing-selected subhalos (Figures 7 and 8). The NFW and TNFWProb models are then applied to describe the profile, and these two models (Table 7) give an acceptable fit. The best-fit tangential profile for the TNFWProb model is similar to that for the NFW model, because the intrinsic distribution of r_t makes a sharply truncated profile blunt. The mean virial radius for the NFW model, $273.87_{-45.98}^{+58.80} h^{-1}$ kpc, is larger than the mean truncation radius $\langle r_t \rangle = 60.84_{-15.34}^{+7.62} h^{-1}$ kpc for the TNFWProb model. On average, three luminous galaxies are inside the mean virial radius of luminous galaxies. In other words, the mass distribution of subhalos associated with luminous galaxies overlap each other. The NFW model is therefore unlikely to represent halos associated with luminous member galaxies. On the other hand, the TNFWProb model gives a large scatter of the truncation radius compared to the mean value, $\sigma_{r_t}/\langle r_t \rangle \sim 37\%$. A broad distribution of the truncation radius smooths the truncation feature in the mean tangential profile for a large sample of less massive subhalos, which makes it difficult to resolve the subhalo size. To confirm this explanation, we conducted a stacked lensing analysis using a mock shear

Table 7
Best-fit Mass Profile Parameters for NFW and TNFWProb Models, Obtained by Galaxy–Galaxy Lensing for Luminous Member Galaxies

Number ^a	$\langle M_{\text{sub}} \rangle^b$ ($10^{12} h^{-1} M_{\odot}$)	$\langle r_t \rangle^b$ (h^{-1} kpc)	$\sigma_{r_t}^b$ (h^{-1} kpc)	$M_{\text{vir}}^{\text{NFWc}}$ ($10^{12} h^{-1} M_{\odot}$)	c_{vir}^c	$\langle L_{i'} \rangle^d$ ($10^{10} h^{-2} L_{\odot}$)	S/N ^e
64	$1.10^{+0.40}_{-0.40}$	$60.84^{+7.62}_{-15.34}$	$22.56^{+19.47}_{-10.64}$	$2.39^{+1.89}_{-1.01}$	$22.99^{+20.25}_{-9.81}$	2.25	5.63

Notes.

^a Number of luminous member galaxies selected by luminosities ($L_{i'} > 10^{10} h^{-2} L_{\odot}$) and cluster-centric radii ($10' \leq r \leq 80'$).

^b Best-fit mass, the average and standard error of truncation radius distribution for the TNFWProb model.

^c Best-fit virial mass and halo concentration for the NFW model.

^d Average luminosity ($L_{i'}$).

^e Signal-to-noise ratio for the tangential distortion profile.

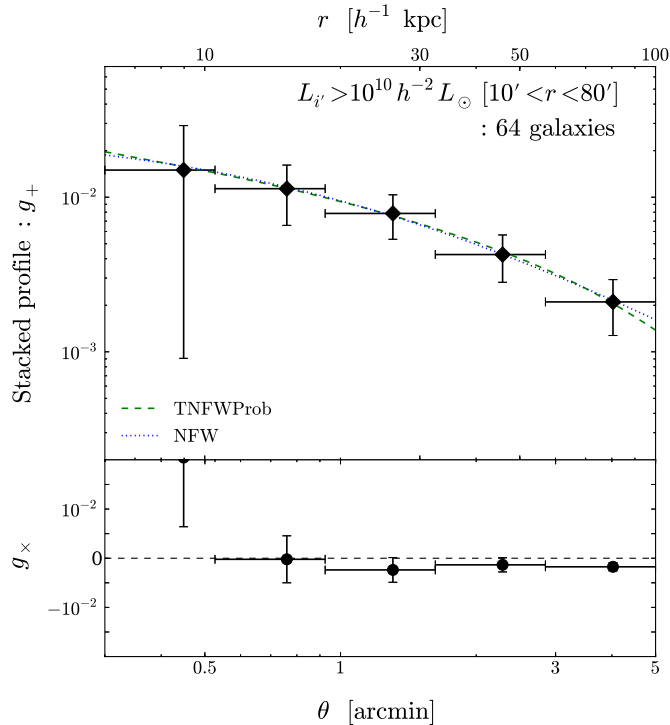


Figure 10. Mean distortion profile for 64 luminous member galaxies with luminosities more than $10^{10} h^{-2} L_{\odot}$. The red solid, green dashed, and blue dotted curves are the best-fit TNFW, TNFWProb, and NFW models, respectively.

(A color version of this figure is available in the online journal.)

catalog (Table 6) in the same way as Section 3.4.5. We found that the truncation feature in the stacked profile is obscured and the mock simulation recovers the input values. Although we also conducted fitting stacked profiles for subsamples divided by luminosities or projected distances from the cluster center, only the upper limits can be derived. We also checked less luminous galaxies with luminosities less than $10^{10} h^{-2} L_{\odot}$ but found significant contamination from neighboring luminous or less luminous galaxies in the mean tangential profile.

Previous studies (Natarajan & Springel 2004; Natarajan et al. 2007, 2009; Limousin et al. 2005, 2007) conducted galaxy–galaxy lensing studies for clusters at $z \gtrsim 0.2$ using single-band images. As described by Broadhurst et al. (2005) and Okabe et al. (2010b, 2013), lensing signals would be significantly diluted by a contamination of unlensed member galaxies in the shear catalog. Their catalog for background source galaxies using the single filter would suffer from a contamination of member galaxies. It is thus difficult to make a fair comparison between our result and the previous studies.

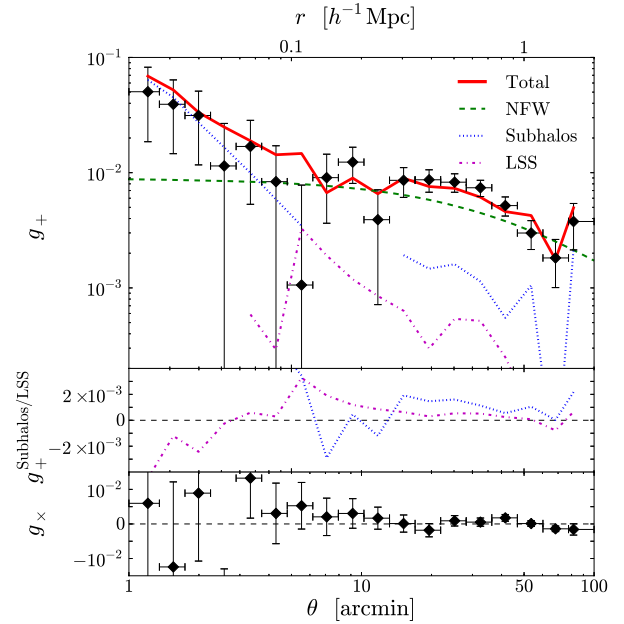


Figure 11. Top panel: The tangential distortion component, g_+ , with respect to the projected cluster-centric radius, in the range of 1–100 arcmin, is estimated by azimuthally averaging the measured galaxy ellipticities. The green dashed, blue dotted, and magenta dashed-dotted lines are the best-fit NFW profile as the smooth mass component of the main cluster, lensing signals expected from subhalos, and the LSS lensing model, respectively. The total lensing signal (red solid line) of the three components is consistent with the observed distortion profile. Middle panel: The tangential profiles for subhalos (blue dotted) and the LSS lensing model (magenta dashed-dotted), are the same as that in the top panel, except for the use of a linear scale. Bottom panel: The 45° rotated component, g_\times , is consistent with a null signal.

(A color version of this figure is available in the online journal.)

5. MAIN CLUSTER MASS MEASUREMENT

A tangential distortion profile, g_+ , with respect to the cluster center, is a powerful tool to estimate the cluster mass (Okabe et al. 2010b). The tangential distortion profile as a function of the projected cluster-centric radius is computed by azimuthally averaging the measured galaxy ellipticities. Here, we assume that the cluster center is at the central position of the subhalo “21” associated with the cD galaxy (NGC 4874). The top panel of Figure 11 shows a complex feature of the lensing profile in the radial range of $1'–100'$, extending over 2 orders of magnitude. Here, the data points are calculated using the shear catalog without the LSS modeling. The lensing signal changes from $\mathcal{O}(10^{-1})$ to $\mathcal{O}(10^{-3})$ as the radius increases. As expected from the low lensing efficiency of the nearby cluster, the lensing signal is 1 order of magnitude lower than that for massive clusters at $z \sim 0.2$ (e.g., Okabe et al. 2010b). However, the S/N reaches

Table 8
Main Cluster Mass Estimates

Fitting Method ^a	M_{vir} ($10^{14} h^{-1} M_{\odot}$)	c_{vir}	M_{200} ($10^{14} h^{-1} M_{\odot}$)	c_{200}	M_{500} ($10^{14} h^{-1} M_{\odot}$)	M_{1000} ($10^{14} h^{-1} M_{\odot}$)	M_{2500} ($10^{14} h^{-1} M_{\odot}$)
g_+ profile	$8.42^{+4.17}_{-2.42}$	$3.57^{+1.54}_{-1.12}$	$6.23^{+2.53}_{-1.58}$	$2.55^{+1.17}_{-0.84}$	$3.89^{+1.04}_{-0.76}$	$2.47^{+0.44}_{-0.37}$	$1.15^{+0.22}_{-0.22}$
ζ_c profile	$8.31^{+2.42}_{-1.82}$	$3.24^{+0.80}_{-0.67}$	$6.08^{+1.51}_{-1.20}$	$2.30^{+0.61}_{-0.50}$	$3.67^{+0.69}_{-0.60}$	$2.27^{+0.36}_{-0.33}$	$1.00^{+0.18}_{-0.18}$

Note. ^a Profiles for fitting.

S/N $\simeq 13.3$ thanks to a remarkably large number of background galaxies, which is comparable to or higher than those of clusters at $z \sim 0.2$ (Okabe et al. 2010b). This high S/N validates weak-lensing analysis for low redshift clusters ($z \lesssim 0.1$) which have been overlooked for a long time. We also find that the 45° rotated component, g_\times (bottom panel of Figure 11), which is a non-lensing mode serving as a monitor of systematics errors, is 1 order of magnitude smaller than the lensing mode, g_+ , which is consistent with a null signal.

The tangential distortion contains complete information for the lensing signals, including the smoothed mass component of the main cluster, the interior substructure (Section 3.2), and LSS lensing signals behind the cluster (Section 2.6). To understand the profile, we computed the tangential shear profiles for 32 shear-selected subhalos and the LSS lensing model, illustrated by the blue dotted and magenta dashed-dotted lines in the top and middle panels of Figure 11. The S/N for the subhalos is S/N $\simeq 4.4$, accounting for 33% of the total distortion signal. This indicates that the profile highly resolves the lensing signal from the interior substructure by the large apparent size of the cluster. The observed signal in the central region ($r \lesssim 5'$) is dominated by the subhalo “21.” The lensing signals in $5' \lesssim r \lesssim 12'$ and in $r \sim 70'$ are depressed by prominent subhalos. As for LSS lensing, the signal-to-noise ratio is S/N $\simeq 1.3$. Here, since the LSS lens modeling for possible background groups, “F” and “I” (Table 2 and Figure 3), has failed significantly, we estimated the lensing distortion pattern from the NFW profile determined by the tangential profile for this object and found that this background group depresses the observed lensing signal at $r \sim 70'$.

We fit a single NFW model to the distribution profile corrected using the LSS lensing model. The lensing signals from the subhalos gradually change from positive to negative in the central region ($\lesssim 12'$). These absolute values account for a large fraction of the total lensing signals, which makes it difficult to discriminate between signals from the subhalos and the main cluster based on the central signals. Indeed, when a single NFW model fits the data, the best-fit halo concentration is systematically changed ($\Delta c_{\text{vir}} \lesssim 1$) by a choice of the innermost radius. To avoid the subhalo bias in cluster mass measurements, we estimate the radial range for the fitting, by requiring that the fraction of the absolute value of subhalo signals to observed signals is less than 30%. We fit the tangential profile between $13'$ ($\sim 260 h^{-1} \text{kpc}$) and $64'$ ($\sim 1.3 h^{-1} \text{Mpc}$) with a single NFW model. Here, the physical scale of the innermost radius is comparable to those for massive clusters at $z \sim 0.2$ (Okabe et al. 2010b). The resultant masses at different overdensities are listed in Table 8. The virial mass and concentration are $M_{\text{vir}} = 8.42^{+4.17}_{-2.42} \times 10^{14} h^{-1} M_{\odot}$ and $c_{\text{vir}} = 3.57^{+1.54}_{-1.12}$, respectively.

We also fit the profile in the full range with the NFW model for the smooth matter component and a central point mass contribution of the brightest cluster galaxy (BCG). We obtain the

point mass $M_{\text{pt}} = 5.67^{+0.32}_{-0.32} \times 10^{12} h^{-1} M_{\odot}$, which is consistent with the projected mass measurement of subhalo “21” (Table 3). The summation of the virial mass and the point mass is $M_{\text{tot}} = 8.21^{+2.99}_{-1.98} \times 10^{14} h^{-1} M_{\odot}$. The total mass is in agreement with the estimated virial mass derived using the tangential fit for the radial range to minimize subhalo contributions.

We next repeat fitting with the NFW model as the smooth component, by fully taking into account lensing signals from all shear-selected subhalos and the LSS lensing model. The best-fit profile for the smooth component is shown in the green dashed line in Figure 11. The total signal (red solid line) from three different components of the smooth NFW profile, subhalos and LSS lens model describes the observed signals remarkably well. The summation of the virial mass and subhalo masses, $M_{\text{tot}} = 8.18^{+3.78}_{-2.02} \times 10^{14} h^{-1} M_{\odot}$, is in good agreement with the virial mass M_{vir} (Table 8). A singular isothermal sphere (SIS) model is strongly disfavored as the smoothed mass component, returning a goodness-of-fit statistic of $\chi^2_{\text{min}}/\text{d.o.f.} = 59.3/11$.

We also conduct the cluster mass measurement using the LSS error covariance matrix (e.g., Schneider et al. 1998; Hoekstra 2003), as described in Section 3.4.2. Although the error covariance matrix does not significantly change the result of subhalo mass measurement, the situation for the cluster mass measurement is slightly different. The diagonal component of the LSS error covariance matrix becomes comparable to the statistical error for $r \gtrsim 50'$. The S/N estimated from the covariance matrix in the tangential shear profile becomes smaller S/N $\simeq 7.5$ from the case of the statistical errors because the LSS errors in different radial bins are correlated. The S/N is consistent with Hoekstra (2003). We use the shear catalog without the correction of the LSS model in the full radial range of the cluster and apply the NFW model for the smooth matter component and a central point source of the BCG. The best-fit mass is $M_{\text{tot}} = 8.80^{+7.59}_{-3.74} \times 10^{14} h^{-1} M_{\odot}$. The upper and lower errors become larger by $\sim 80\%$ and $\sim 40\%$, respectively.

The projected mass (M_{ζ_c}) measurement (ζ_c statistics) for the main cluster is less sensitive to lensing signals from subhalos, because it estimates a cumulative profile. It is thus complementary to the tangential fit. Figure 12 shows the M_{ζ_c} profile calculated with the fixed background annulus of $70' - 90'$. The background region is inside the best-fit virial radius ($r_{\text{vir}} = 96.67^{+13.89}_{-10.32} \text{ arcmin}$) derived from the tangential shear fit. Following Okabe & Umetsu (2008), we fit the ζ_c profile with a single NFW model, taking into account the error covariance matrix. The best-fit profile is shown by the red solid line. The best-fit values (Table 8) are consistent with those for the tangential shear fit.

We compare the best-fit mass and concentration with results in the literature (Table 9). The mass measurements in this study are consistent with our previous analysis (Okabe et al. 2010a). The statistical precision of the new mass estimates is improved by four times thanks to the huge number of background galaxies. Gavazzi et al. (2009) conducted fitting the tangential distortion

Table 9
Mass and Concentration Previously Reported in the Literature

Reference	M_{vir} ($10^{14} h^{-1} M_{\odot}$)	c_{vir}	M_{200} ($10^{14} h^{-1} M_{\odot}$)	c_{200}
WL : (Kubo et al. 2007)	$18.8^{+6.5}_{-5.6}$	$3.84^{+13.16}_{-1.84}$
WL : w/o priors ^a (Gavazzi et al. 2009)	$4.27^{+8.47}_{-2.45}$	$6.7^{+4.1}_{-3.3}$	$3.57^{+3.01}_{-1.47}$	$5.0^{+3.2}_{-2.5}$
WL : w/ priors ^a (Gavazzi et al. 2009)	$7.77^{+11.69}_{-4.27}$	$4.9^{+1.7}_{-1.4}$	$6.79^{+4.27}_{-2.45}$	$3.5^{+1.1}_{-0.9}$
WL : (Okabe et al. 2010a)	$8.92^{+20.05}_{-5.17}$	$3.50^{+2.56}_{-1.79}$	$6.61^{+12.06}_{-3.63}$	$2.50^{+1.94}_{-1.34}$
Dynamics : (Rines et al. 2003)	7.85	...
Dynamics : (Łokas & Mamon 2003)	8.45 ± 3.15	9.4

Note. ^a Priors with and without the mass-concentration relation.

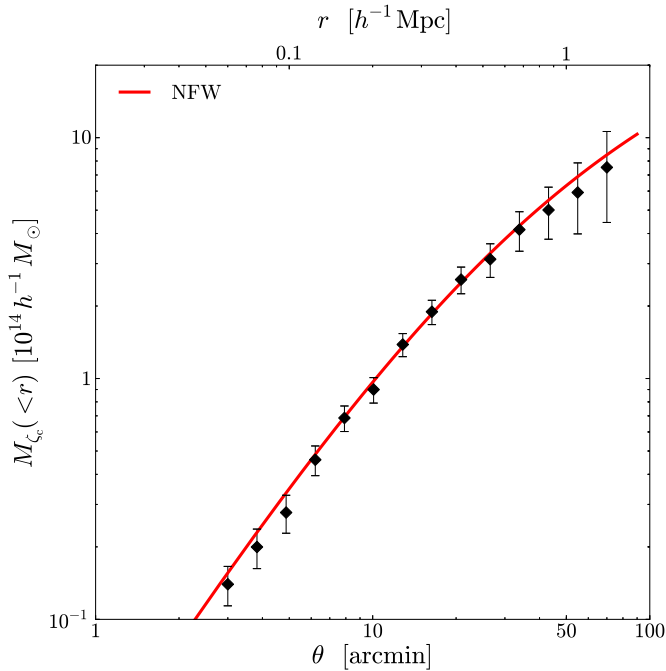


Figure 12. M_c profile as a function of the projected cluster-centric radius, estimated by azimuthally averaging galaxy ellipticities with a correction factor from the LSS lens model. The red solid line is the best-fit NFW profile.

(A color version of this figure is available in the online journal.)

profile in the range of $0'.35 \lesssim r \lesssim 35'$ using the NFW model including and excluding priors on mass and concentration relations, using CFHT/Megacam data. In that study, the LSS lensing effect was not accounted for. The best-fits, regardless of priors, are compatible within their large errors, with the present study. However, their lensing signals (Figure 3 in Gavazzi et al. 2009) differ from the results in the present study (Figure 11). Their profile ($0'.35 \lesssim r \lesssim 35'$) is well described by a single NFW model. The lensing signals in the same radial range in the present study are dominated by prominent subhalos in $r \lesssim 12'$ and by the smooth mass component in $12 \lesssim r \lesssim 35'$, respectively. We conduct the tangential fit using the profile computed with the same radial bins as Gavazzi et al. (2009) and a single NFW model and obtain only an upper limit on $M_{\text{vir}} < 4 \times 10^{16} h^{-1} M_{\odot}$ because of an inadequate model. Kubo et al. (2007) carried out weak-lensing analysis using SDSS data. The best-fit M_{200} (Kubo et al. 2007) derived by fitting the tangential profile up to $10 h^{-1} \text{Mpc}$ with a single NFW model is three times higher than that observed here. The background LSS lensing effect was not accounted for in that study. Since

their outermost radius ($10 h^{-1} \text{Mpc}$) is five times higher than our best-fit virial radius, their mass would be overestimated by mass distribution outside the cluster. The dynamical mass estimates of M_{vir} and M_{200} (Rines et al. 2003; Łokas & Mamon 2003) agree with our best-fits, although their concentration is three times higher than estimates in the present study.

6. DISCUSSION

6.1. Subhalo Mass Function

The subhalo mass function is computed from Monte Carlo redistributions of subhalo masses taking into account both measurement uncertainties and the systematic error on the applied threshold (Section 3.4.4). Figure 13 shows the subhalo mass function. The error bars are based on both measurement and systematic errors. The resulting subhalo mass function covers over 2 orders of magnitude in mass. The number of subhalos decreases as their mass increases, while it is significantly decreased in the low-mass end ($M_{\text{sub}}/M_{\text{vir}} \sim 10^{-3}$) because the detection limit appeared in the mass map. To access the purity, we also compute the mass function of spurious peaks, $dN_{\text{fake}}/d \ln M_{\text{fake}}$. Here, we calculate the mass function for spurious peaks, using the probability distribution of best-fit masses, M_{fake} , derived by stacked lensing analysis (Section 3.4.3). The number of false peaks as a function of the mass is given by $N(M_{\text{fake}}) = N_{\text{fake}} \sum_i N_{\text{sample},i} P_i(M_{\text{fake}}) / \sum_i N_{\text{sample},i}$, where N_{fake} is the total number of spurious peaks and $P_i(M_{\text{fake}})$ and $N_{\text{sample},i}$ are the probability distribution and the subhalo number for the subsamples of the mass bin, respectively. The probability distribution, $P_i(M_{\text{fake}})$, is calculated by the best-fit masses taking into account the measurement uncertainty. The green dashed lines show a single peak of the mass function for spurious peaks. The functional form is different from the observed mass function. The peak height of spurious peaks is 1 order of magnitude lower than the observed mass function in the same mass range. Stacked lensing analysis of false peaks (Section 3.4.3) disfavors the contamination of spurious peaks in the sample of subhalos. Even if they exist, the contamination level is negligible for a study of the mass function.

We fit the subhalo mass function with single power law model (e.g., Gao et al. 2012),

$$dn/d \ln M_{\text{sub}} \propto M_{\text{sub}}^{-\alpha} \quad (5)$$

and a Schechter function (e.g., Schechter 1976; Shaw et al. 2006),

$$dn/d \ln M_{\text{sub}} \propto M_{\text{sub}}^{-\beta} \exp(-M_{\text{sub}}/M_*). \quad (6)$$

The mass function is modified from these analytical functions

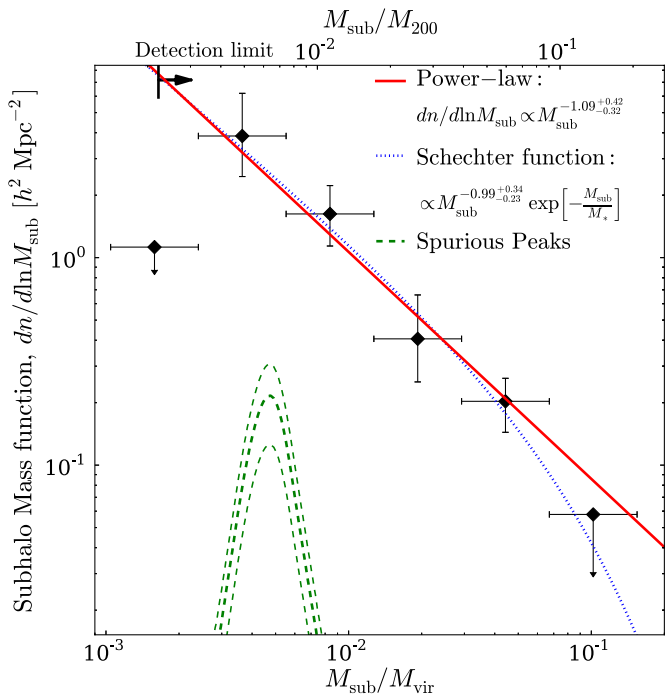


Figure 13. Subhalo mass function spanning 2 orders of magnitude of subhalo masses. The red solid and blue dotted lines are the best-fit power-law model and Schechter function, respectively. The best-fit powers are in remarkable agreement with CDM predictions. Green dashed lines are the mass function for spurious peaks. The thick and thin dashed lines are the best-fit and the 68% C.L. uncertainty, respectively.

(A color version of this figure is available in the online journal.)

because of finite measurement errors for the subhalo masses. This corrects the modeling for the so-called Eddington bias. The model of the mass function is described by the convolution between the analytical forms and the errors, $dn_{\text{model}}/d \ln M_{\text{sub}} = \int dn/d \ln x p(x, M_{\text{sub}}) dx / \int p(x, M_{\text{sub}}) dx$. Here, we assume a Gaussian probability function, $p(x, M_{\text{sub}}) = \sum_i \exp(-(x - M_{\text{sub},i})^2 / 2\sigma_{M,i}^2) / (2\pi\sigma_{M,i}^2)^{1/2}$, where $M_{\text{sub},i}$ and $\sigma_{M,i}$ are the mass estimate and the error for i th subhalo, respectively. The cutoff mass, M_* , in the Schechter function is sensitive to abundance at the high-mass end. However, since the abundance of massive subhalos is small, it is not well constrained, $M_*/M_{\text{vir}} = 0.089^{+0.135}_{-0.064}$. We are therefore unable to discriminate between the single power law and the Schechter function. The best-fit power indices, which characterize the shape of the function at the intermediate and low ranges, are in good agreement ($\alpha = 1.09^{+0.42}_{-0.32}$ and $\beta = 0.99^{+0.34}_{-0.23}$). We also computed a subhalo mass function including four subhalo candidates with no optical counter and obtain the best-fit $\alpha = 1.15^{+0.38}_{-0.32}$ and $\beta = 0.99^{+0.38}_{-0.24}$. For further verification, we excluded the most and least massive of the massive subhalos to construct a mass function and found that the best-fit slope values do not significantly change. The best-fit slopes are in remarkable agreement with CDM predictions ~ 0.9 – 1.0 from numerical simulations (e.g., Diemand et al. 2004; De Lucia et al. 2004; Gao et al. 2004b, 2012; Shaw et al. 2006; Angulo et al. 2009; Giocoli et al. 2010; Klypin et al. 2011) and analytical models (e.g., Taylor & Babul 2004; Oguri & Lee 2004; van den Bosch et al. 2005; Giocoli et al. 2008). A recent high-resolution numerical simulation study (Gao et al. 2012) found that the slope of mass function in the range of $10^{-6} < M_{\text{sub}}/M_{200} < 10^{-3}$ gives $\alpha = 0.98$.

The mass fraction for observed subhalos is estimated as $f_{\text{sub}} = \sum_i M_{\text{sub},i}/M_{\text{vir}} = 0.226^{+0.111}_{-0.085}$ with the tangential fit for the main cluster and $f_{\text{sub}} = 0.229^{+0.078}_{-0.064}$ with ζ_c fit, respectively. Shaw et al. (2006) estimated the mean mass fraction as a function of the virial mass, $\langle f_{\text{sub}} \rangle = 0.14 \pm 0.02 (M_{\text{vir}}/8 \times 10^{14} h^{-1} M_{\odot})^{0.44 \pm 0.06}$. The mass fraction for the Coma cluster is larger than the mean fraction, $\langle f_{\text{sub}} \rangle = 0.16$, estimated using the best-fit virial mass. We also calculated the mass fraction within r_{200} , $f_{\text{sub},200} = 0.222 \pm 0.077$.

6.2. Correlation between Subhalo Masses and Truncation Radii

It is interesting to investigate the correlation between the subhalos' masses and truncation radii, because they are both free parameters in stacked lensing analysis. We compile the stacked lensing results divided by mass and cluster-centric bins and find a tight correlation of $M_{\text{sub}} \propto r_t^{1.18^{+0.10}_{-0.09}}$ and $M_{\text{sub}} \propto r_t^{1.19^{+0.17}_{-0.16}}$ for the TNFW and TNFWProb models, respectively. Considering a functional form of the NFW model, $M_{\text{NFW}}(< x) \propto \log(1+x) - x/(1+x)$ (Equation (D2)) where $x = r/r_s$ is the radius normalized by a scale radius, the best-fit slope values imply that the mass loss occurs in the subhalo outskirts beyond the scale radius as long as the internal structure does not change during movement in the host halo.

6.3. Radial Dependence of Subhalo Properties

Subhalos captured by more massive halos are subject to dynamical friction, losing their angular momentum and subsequently falling inward the center. Simultaneously, their masses are reduced by the tidal force which increases with an increasing radius from the cluster center. The subhalos in the central region have been affected by the tidal field for a longer time than those on the outskirts. It is thus expected that the subhalo mass and truncation radius are an increasing function of cluster radius. The survey of subhalos using the wide-field imaging data allows us to study the radial dependence of their properties. For this purpose, we use the projected position of shear-selected subhalos. It is difficult to constrain the pericenter radius and a line-of-sight position of the subhalo. In order to reduce these uncertainties, we compute the mean subhalo masses and truncation radii derived from stacked lensing analyses for the subsample divided by their positions from the cluster center (Section 3.3). The mean projected distance of the subsample is estimated as a weighted average of projected distances from the cluster center for the individual subhalos. The weight function is given by the tangential distortion signals with respect to the subhalo center. The left and right panels of Figure 14 display a clear radial dependence of subhalo masses and truncation radii, as expected from tidal destruction. The subhalo masses and radii gradually increase out to $\sim 1 h^{-1} \text{Mpc}$ and drastically rise due to massive subhalo “32” on the outskirts in the range of 1.2–1.6 $h^{-1} \text{Mpc}$. We fit the subhalo mass profile with a functional form of $\log(M_{\text{sub}}/M_{\text{pivot}}) = A + B \log(r/r_{\text{pivot}})$ where $M_{\text{pivot}} = 10^{12} h^{-1} M_{\odot}$ and $r_{\text{pivot}} = 1 h^{-1} \text{Mpc}$ and obtain, $A = 2.66 \pm 0.08$ and $B = 1.45 \pm 0.12$. The best-fit parameters for the inner three bins are $A = 1.86 \pm 0.23$ and $B = 0.55 \pm 0.26$. The subhalo size profile is fitted with $\log(r_t/r_{t,\text{pivot}}) = A + B \log(r/r_{\text{pivot}})$ and $r_{t,\text{pivot}} = 1 h^{-1} \text{kpc}$. The best-fit parameters for all, and for the three inner bins, are $A = 4.95 \pm 0.04$ and $B = 1.18 \pm 0.08$, and $A = 4.07 \pm 0.26$ and $B = 0.38 \pm 0.24$, respectively. The best-fit slope values for

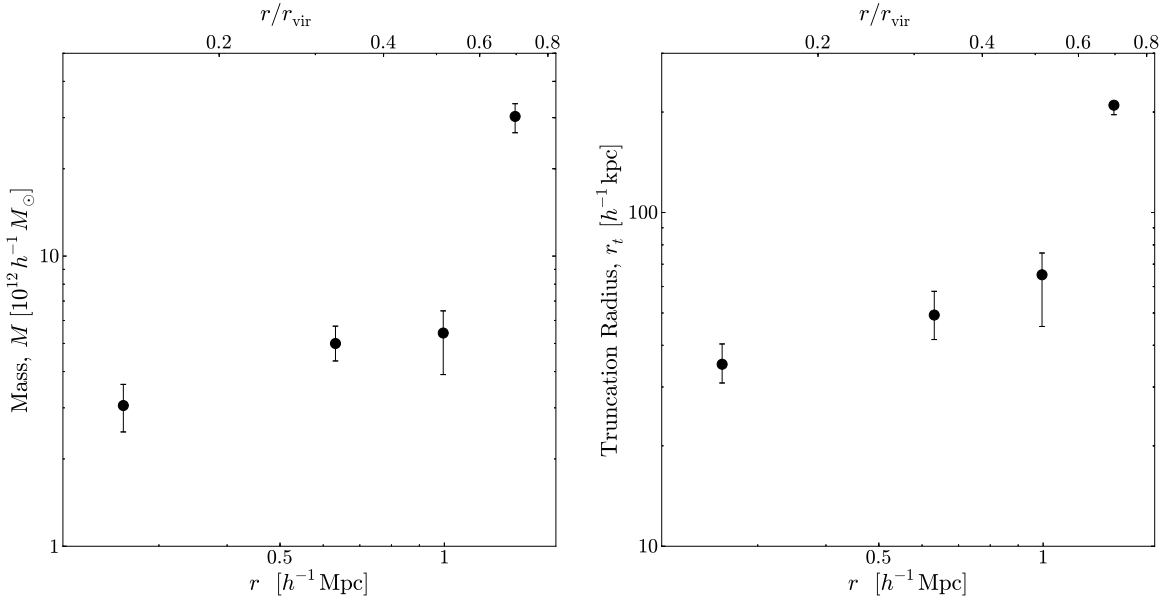


Figure 14. Mass (left) and truncation radius (right) profiles of subhalos as a function of the projected cluster-centric radius. The black circles represent the masses and truncation radii of subhalos using stacked weak-lensing analysis for lensing-selected subhalos, showing that they monotonically increase with an increasing radius.

the mass and truncation radius are significantly changed by the presence of the massive subhalo on the outskirts ($60' < r < 80'$). The similar trend on the half mass radius for subhalos in simulated clusters are found by Limousin et al. (2009).

The tidal radius of subhalos is generally defined by a competition between the differential tidal forces of the host halo potential and the acceleration toward the subhalos. Equivalently, this condition can be rewritten as a balance between the average density of subhalos and the host halo, $\bar{\rho}_{\text{sub}} = \eta \bar{\rho}_{\text{main}}$, where η is an efficiency factor. For instance, $\eta = 3$ for a point mass case on a circular orbit, $\eta = 2$ for the Roche limit, and $\eta = 2 - d \ln M_{\text{main}} / d \ln R$ in the case of extended mass profiles of subhalos and the host halo (e.g., Tormen et al. 1998; Taylor & Babul 2004; Gan et al. 2010) in a linear regime of $M_{\text{sub}}/M_{\text{main}} \ll 1$ and $r_i/R \ll 1$, where R is the pericenter radius from the cluster center. The minimum subhalo size is determined by the pericenter radius. Although we cannot constrain the pericenter radius of subhalos from the current position of the subhalos, it is interesting to compare the density ratio, η , with these trial approximations. We calculate the mean densities for subhalos, $\bar{\rho}_{\text{sub}} = M_{\text{sub}}/r_i^3$, and for the host halo, $\bar{\rho}_{\text{main}} = M_{\text{NFW}}(<R)/R^3$, where M_{NFW} is a spherical NFW mass enclosed within the three-dimensional radius. Here, we use the best-fit NFW model and the projected cluster-centric radius for subhalos. The mean density for subhalos is higher than that for the cluster mass. The density ratios, $\eta \sim 10\text{--}40$ for shear-selected subhalos (Section 3.3) and ~ 10 for luminous galaxies (Section 4), are comparable to each other, but they are higher than expected by the linear regime assuming that the current position is the pericenter. If the discrepancy could be explained by a difference of the positions, shear-selected subhalos and luminous galaxies would be located inward. On the other hand, the subhalo mass implies that the detected subhalos are remnants of group-scale structure. Large and massive subhalos would not be described by the linear regime.

6.4. Surface Number Density for Subhalos

It is important to estimate a surface number density profile for subhalos to understand the evolution of subhalos in the cluster. Figure 15 shows the surface number density profile of

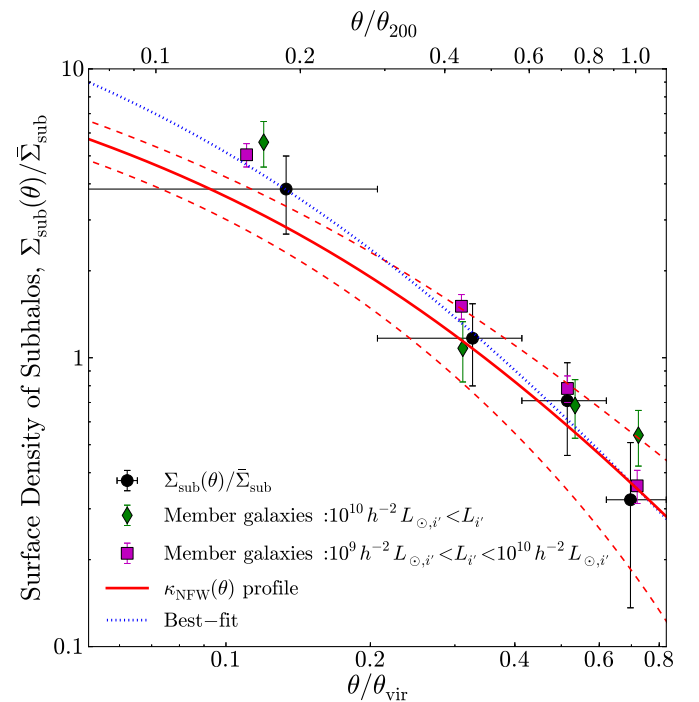


Figure 15. Surface density (black circles) profile of subhalos. The best-fit profile is shown by a blue dotted line. For comparison, a red solid line shows the surface mass density for the total mass of the main cluster, normalized with the number density at r_{200} . Red dashed lines are the 68% confidence uncertainties for the total mass. Green diamonds and magenta squares denote the surface mass densities for member galaxies of which luminosities are $L_{i'} > 10^{10} h^{-2} L_{\odot,i'}$ and $10^9 h^{-2} L_{\odot,i'} < L_{i'} < 10^{10} h^{-2} L_{\odot,i'}$, respectively.

(A color version of this figure is available in the online journal.)

subhalos normalized by the mean surface density. The errors for the surface number density are assumed to be Poisson noise. It is clear that the surface number density increases while decreasing the cluster-centric radius. For comparison, we compute the surface number density profiles of member galaxies for which the luminosities are $L_{i'} > 10^{10} h^{-2} L_{\odot,i'}$ and

$10^9 h^{-2} L_{\odot,i'} < L_{i'} < 10^{10} h^{-2} L_{\odot,i'}$. Both profiles are similar to that of subhalos. To quantify these distributions, we assume the spherical symmetric NFW distribution for the subhalos and member galaxies and fit the profiles. The surface number density profile is specified by three parameters including normalization, the concentration and the virial radius. We here use the virial radius determined by the tangential shear fit (Section 5). The best-fit concentrations are $c_{\text{vir}} = 5.73 \pm 4.46$ for subhalos, $c_{\text{vir}} = 5.97 \pm 3.28$ for luminous galaxies and $c_{\text{vir}} = 5.35 \pm 1.00$ for less luminous galaxies. All best-fit concentrations agree with each other. We also compute the surface mass density profile for the total mass from the best-fit NFW parameters (Section 5). Here, the normalization is set to be the surface density of the subhalos at r_{200} . The best-fit concentrations for the subhalos and luminous member galaxies do not differ from that for the main mass, while the less luminous galaxies are more centrally concentrated. Recent numerical simulations (e.g., Ghigna et al. 2000; Diemand et al. 2004; De Lucia et al. 2004; Gao et al. 2004b, 2012, 2004a; Nagai & Kravtsov 2005) and analytical models (e.g., Taylor & Babul 2005b; Zentner et al. 2005) have shown that the radial distribution of subhalos is less concentrated than that of the total mass, because the subhalos lose their mass more efficiently in the inner regions of the main halo. The local surface density of subhalos is noisy, and there is an uncertainty in their position along the line-of-sight. The Coma cluster contains the famous NGC 4839 group in the southwest central region (Figure 3), and thus, the presence of subhalos in the southwest direction from the cluster center might significantly affect the surface profile. We thus need further studies to measure the subhalo distribution and compare these with the dark matter distribution of the main cluster, using a large sample of clusters, especially nearby clusters.

6.5. Mass-to-light Ratio

The evolution of galaxies is profoundly affected by their surrounding environments, such as the presence of dark matter halos. The environmental processes (e.g., Boselli & Gavazzi 2006) in an overdensity region such as groups or clusters consume cold gasses in galaxies through star-bursts triggered by mergers, tidal interaction with other galaxies, and ram-pressure stripping by the gas, which leads to a halt in star formation. Based on hierarchical structure formation scenarios, some cluster galaxies have spent a long time in group-scale environments, before being captured in their current host halo. These group-scale environments may play an important role in the evolution of the galaxies, rather than that of the cluster environment (Zabludoff & Mulchaey 1998). On the other hand, subhalo masses and sizes depend on their initial properties, infall epochs and subsequent evolution in the cluster halo. Therefore, study of a galaxy-dark matter connection may provide insights into how galaxies form and evolve with different mass properties. We compare two independent quantities of weak-lensing masses of subhalos and luminosities for associated galaxies. It is well established observationally that there is a correlation between luminosity, velocity dispersion, and scale length for early type galaxies, the so-called fundamental plane (Djorgovski & Davis 1987; Dressler et al. 1987). These studies estimate dynamical mass tracing the gravitational potential of a galaxy at small scales. Weak-lensing analysis measures the mass of dark matter where the distribution extends beyond the galaxies. Thus, our approach is complementary to previous studies (e.g., Cappellari et al. 2006; Cody et al. 2009). We compile two stacked lensing results of shear-selected subhalos divided by

individual masses (TNFW; Section 3.3) and luminous member galaxies (Section 4). Here, we use the truncated mass rather than the NFW model. The luminosity of each sample is estimated by an average over all galaxies associated with the subhalos, with a weight of the tangential distortion signals. We plot the correlation between the subhalo masses and the galaxy luminosities in the left panel of Figure 16. The luminosity ranges between 10^{10} – $10^{11} h^{-2} L_{\odot}$, indicating that member galaxies in the subsamples are mainly composed of elliptical galaxies. The mass increases with increasing luminosity. To quantify this trend, we fit with $\log(M_{\text{sub}}/M_{\text{pivot}}) = A + B \log(L_{i'}/L_{\text{pivot}})$, where $L_{\text{pivot}} = 10^{10} h^{-2} L_{\odot}$. The best-fit slope, $B = 1.49 \pm 0.16$, gives a positive slope at an 8σ level. The normalization is $A = -0.15 \pm 0.19$. The data points show a large amount of scatter. To understand the scatter, further careful study using other parameters of galaxies is needed to constrain the fundamental plane between the subhalo masses and the galaxy properties. We convert the scaling relation into the mass-to-light ratio, $M/L = 86.1^{+18.1}_{-15.0} (L_{i'}/10^{10} h^{-2} L_{\odot})^{0.49 \pm 0.16} [h M_{\odot}/L_{i',\odot}]$. Limousin et al. (2009) have investigated the scaling relation between the luminosity and the total mass in simulated clusters and found $M_{\text{tot}} \propto L^{1.431 \pm 0.119}$ in the massive cluster ($M_{\text{vir}} = 1.3 \times 10^{15} h_{70}^{-1} M_{\odot}$) at $z = 0$, which is in a good agreement with our result. We compare this analysis to the mass-to-light ratio determined by dynamical masses. Cappellari et al. (2006) estimated the scaling relation of $M/L = (2.35 \pm 0.19)(L_{i'}/10^{10} L_{i',\odot})^{0.32 \pm 0.06}$ for the SAURON sample. Our normalization is higher by 1 order of magnitude than dynamical estimates. It is likely due to a difference in mass measurements, because weak-lensing analysis measures the mass of dark matter halos extending beyond galaxy scales. Similar results have been reported by van Uitert et al. (2011), who showed that weak-lensing masses within r_{200} are about 10 times larger than dynamical masses.

The right panel of Figure 16 clearly shows decreasing mass-to-light ratio toward the cluster center, similar to the radial dependence of the mass and truncation radius (Figure 14). Here, we use the TNFW mass for subsamples divided by the projected distance from the cluster center (Section 3.3). The luminosity is estimated in the same way as for subsamples divided by mass bins. We fit the form of $\log(M/L/(M/L)_{\text{pivot}}) = A + B \log(r/r_{\text{pivot}})$ to quantify the radial dependence, where $(M/L)_{\text{pivot}} = 1 h M_{\odot}/L_{\odot}$ and $r_{\text{pivot}} = 1 h^{-1} \text{Mpc}$. We obtain $A = 5.76^{+0.13}_{-0.13}$ and $B = 1.35^{+0.08}_{-0.08}$. The upper panel shows the mass-to-light ratio of subhalos normalized by the cluster mass-to-light ratio, $M/L = 337.4^{+140.2}_{-92.5} h [M_{\odot}/L_{i',\odot}]$, within the virial radius derived from the tangential fit. The mass-to-light ratios for subhalos on the outskirts ($0.7 \lesssim \theta/\theta_{\text{vir}} \lesssim 1$) are close to unity, while the ratios in the central region account for 17%. This feature is explained by a scenario where the dark matter subhalos are more subjected to mass loss due to tidal truncation than luminous galaxies which tend to be in the central region of subhalos. Furthermore, since the mean luminosity increases toward the cluster center, it is also associated with galaxy evolution. Similar trends are suggested by numerical simulations (Springel et al. 2001). They found that the median mass-to-light ratio gradually increases out to 1.5 – $2 h^{-1} \text{Mpc}$ and is saturated beyond that point. Gao et al. (2004a) also found a similar result, where the median mass-to-light ratio for subhalos is saturated beyond r_{200} . The saturated values (Springel et al. 2001) are $\sim 15\%$ – 20% of the cluster mass-to-light ratio in the B -band. The discrepancy in these ratios might be caused by a difference in the subhalo mass range between their simulations

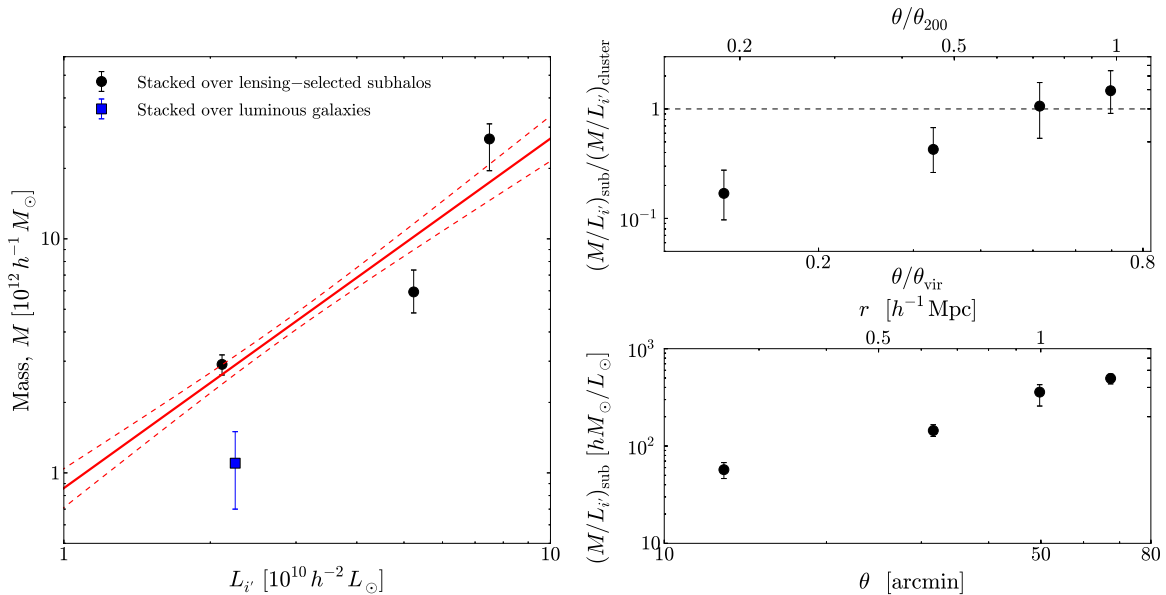


Figure 16. Left panel: The mass and luminosity relation for shear-selected subhalos (black circles) and luminous member galaxies (blue squares). The mass of shear-selected subhalos is from stacked lensing analysis of subsamples divided by model-independent masses. The red solid and dashed lines are the best-fit relationships and 68% confidence level uncertainties, respectively. Right panel: The radial dependence of the mass-to-light ratio obtained from the stacked lensing results for subhalo subsamples divided by their cluster-centric radius. The top panel shows the mass-to-light ratio normalized by the cluster mass-to-light ratio, as a function of the radius normalized by the cluster virial radius (r_{vir} or r_{200}).

(A color version of this figure is available in the online journal.)

and our catalog because we used shear-selected subhalos and they selected cluster galaxies and associated subhalos.

This study suggests that the mass-to-light ratio for cluster subhalos depends on both the luminosity (mass) and the cluster-centric radius. To derive more robust conclusions will require a study using a larger sample of nearby cluster lensing analyses. However, the present results suggest that an assumption of the constant scaling relation between the mass and the luminosity gives a systematic bias on mass measurements and their statistical properties.

6.6. Future Studies

We present a direct observation of the dark matter subhalo mass function using weak gravitational lensing analysis, which is the first evidence for consistency with CDM predictions on cluster sub-scales. It is thus an important step toward studying subhalo mass functions and properties with a large sample of clusters to make stringent tests of the nature of dark matter and the details of structure formation.

Although the subhalo mass function is well described by the single power law or the Schechter function, it is difficult to discriminate between the two functions because the abundance of high-mass subhalos is low. The subhalo mass function stacked over a large sample of clusters will enable us to make a more robust determination of the functional form. Furthermore, the shape of the mass function has a characteristic feature depending on the masses of the other components of dark matter, if any. Thus, the subhalo mass function allows us to constrain the nature of dark matter and structure formation. Hierarchical structure formation predicts that the subhalo mass function depends on host halo mass (e.g., Gao et al. 2004b; van den Bosch et al. 2005; Shaw et al. 2006). Less massive halos form first at higher redshifts where the mean background mass density is higher. Subhalos captured by less massive halos efficiently lose their mass in the high density environment. These subhalos are

furthermore exposed to destruction over a longer time. Less massive halos are therefore expected to contain fewer subhalos. To investigate the parent mass dependence, an increase of sample of clusters is essential. The systematic survey for nearby clusters with these properties will increase the total number of dark matter subhalos on the order of a few hundred or more and improve the statistical accuracy. Furthermore, finer weak-lensing resolution of nearby clusters will enable us to conduct principal component analyses of the properties of dark matter halos/subhalos (e.g., Jeon-Daniel et al. 2011; Skibba & Macciò 2011; Wong & Taylor 2012). Analytical models such as the halo occupation distribution (e.g., Seljak 2000; Cooray & Sheth 2002), the abundance matching (e.g., Vale & Ostriker 2004), and the conditional luminosity function (e.g., van den Bosch et al. 2003) would be helpful to understand the galaxy-dark matter connection.

The near future for multi-wavelength study of subhalos will give us direct and important information on the long-standing problem of the interplay between dark halos and baryons of member galaxies and gasses. We investigated the correlation between galaxy luminosities, subhalo masses and their projected radius from the cluster center. It would also be interesting to investigate the correlation with ages, star formation rates and specific star formation rates of galaxies. Smith et al. (2012) have shown an anisotropic spatial distribution of the galaxies age and found that the older population of galaxies distribute around subhalo “17.” This might suggest that stellar population properties would vary from subhalo-to-subhalo because some cluster galaxies spent a long time in group scale environments before being captured by the cluster. Further systematic studies using other data-sets, such as stellar masses, star formation rate, specific star formation rate and galaxy types, will provide us with information regarding cluster galaxy evolution.

The *ROSAT* X-ray surface brightness distribution (Figure 5) shows that all shear-selected subhalos do not contain X-ray extended structures. This can be understood in terms of

observational and/or physical effects. First, relatively small X-ray sources are unresolved by the poor PSF of the *ROSAT*. Recent observation (Andrade-Santos et al. 2013) using *Chandra* and *XMM-Newton* satellites with high resolution resolves three X-ray subhalos in the central region that are associated with subhalos “21,” “23,” and “24,” respectively. Subhalo masses were estimated under the assumption of hydrostatic equilibrium and are in good agreement with our mass estimates. However, X-ray subhalos in other shear-selected subhalos are not found even with high resolution data, which is due to various physical processes on gas initially bound in the subhalos. Tormen et al. (2004) has pointed out using numerical simulations that the gaseous components, which is collisional matter, are easily destroyed by ram pressure stripping and hydrodynamic instabilities. Accordingly, the lifetime of the X-ray subhalos is much shorter than those of dark matter subhalos. Furthermore, the temperature of the intracluster medium in the central region (~ 8 keV) is too high to be trapped by subhalos. Since X-ray observation at the outskirts requires stable and low X-ray backgrounds, the *Suzaku* X-ray satellite has a great advantage to search for gas components associated at the outskirts of the subhalos (e.g., Kawaharada et al. 2010; Walker et al. 2012; Sato et al. 2012; Ichikawa et al. 2013) rather than the *ROSAT*. Simionescu et al. (2013) has measured the temperature profile out to $70'$. $\sim 1.4 h^{-1}$ Mpc using the *Suzaku*. The temperature at the outskirts drops down to 2 keV. The sound velocity at this temperature, $c_s \sim 720 (k_B T / 2 \text{ keV})^{1/2} \text{ km s}^{-1}$, is lower than the escape velocity, $v_{\text{esc}} \sim 1500 \text{ km s}^{-1}$, expected from the most massive subhalo, number “32.” The enhancement of gas distribution is thus expected to be detected in this region. However, the *Suzaku* pointings do not fully cover the whole area of the cluster. The X-ray follow-up observation of the subhalo regions provides us with important information regarding the gas evolution and the interplay with subhalos (Tozzi & Norman 2001), and resolves possible systematics on the temperature measurement by gas clumpy structures at the outskirts (Nagai & Lau 2011). The thermal Sunyaev–Zeldovich effect (SZE) observation with different sensitivity from the X-ray is also powerful for gas studies. Indeed, Planck Collaboration et al. (2013) has shown that the SZE map with FWHM = $10'$. Planck Collaboration et al. (2013) detected the excess flux around the NGC 4839 group (subhalo “9”), similar to the *ROSAT* X-ray image.

7. CONCLUSIONS

We conducted a weak-lensing survey of subhalos in the very nearby Coma cluster, with 18 pointing Subaru/Suprime-Cam observations, covering 4 deg^2 and measure the mass of 32 subhalos down to the order of 10^{-3} of the virial mass. We quantified systematic issues relevant to lensing signals from the large-scale structure behind the cluster and the probability of spurious peaks. Our findings are summarized as follows:

1. Weak-lensing analysis for the very nearby Coma cluster offers three important advantages to study cluster subhalos. First, the large apparent size of the subhalos enables us to easily resolve the truncation radii for less massive subhalos. Second, the large apparent area covering the subhalos provides us with a correspondingly large number of background galaxies, which leads to low statistical errors, compensates for low lensing efficiency and achieves a high S/N. Third, subhalos mass measurements do not suffer from contamination in lensing signals from the main cluster and other subhalos, because the subhalos are well separated.

It is acknowledged that this analysis is at a disadvantage in distinguishing cluster subhalos from background group structures, although the LSS lensing effect was accounted for in this analysis. Spectroscopic or photometric redshifts of galaxies are essential to make a secure selection of subhalos. A difference in the models of subhalos and background groups/clusters is also helpful to assess the observed lensing signals.

2. Reconstructed mass maps are associated with the projected distributions of member galaxies and the LSS lensing model at $\sim 7\sigma$ – 14σ , suggesting that the observed shear catalog contains complete information regarding the mass structure of, and behind, the cluster.
3. We discovered 32 cluster subhalos by applying thresholds of peaks which appeared in the mass maps. We estimate the model-independent projected masses of subhalos, ~ 2 – $50 \times 10^{12} h^{-1} M_{\odot}$, where the smooth mass component for the main cluster has been subtracted.
4. Stacked lensing analysis for samples divided by subhalo masses and cluster-centric radii shows a sharply truncated profile. The profile is proportional to $g_+ \propto \theta^{-2}$ outside the truncation radii. This feature is well described by truncated NFW (TNFW) profile rather than the universal NFW profile without any truncations, as expected based on a tidal destruction model. For the two subsamples with the most and least massive of the subhalos, the NFW model is strongly disfavored. The stacked lensing masses are consistent with model-independent masses for the individual subhalos.
5. The cluster galaxy–galaxy lensing analysis for luminous member galaxies shows a curved tangential shear profile which is well fitted by the NFW model or the summation of the truncated NFW model considering a Gaussian distribution of the truncation radius. However, the NFW model is unlikely for subhalo models, because the best-fit virial radius is too large for the subhalo model.
6. The subhalo mass function $dn/d \ln M_{\text{sub}}$ is computed taking into account the systematics of subhalo selection. The mass function in the range of 2 orders of magnitude in mass is well described by a single power law $\propto M_{\text{sub}}^{-\alpha}$ or the Schechter function $\propto M_{\text{sub}}^{-\beta} \exp(-M_{\text{sub}}/M_*)$. These best-fit slope $\alpha = 1.09^{+0.42}_{-0.32}$ and $\beta = 0.99^{+0.34}_{-0.23}$ are in a remarkably good agreement with CDM predictions ~ 0.9 – 1.0 (e.g., Giocoli et al. 2010; Gao et al. 2012). This is the first evidence of consistency with CDM predictions on cluster sub-scales.
7. The subhalo masses, truncation radii, and mass-to-light ratios decrease toward the cluster center, as expected from tidal destruction. The galaxy luminosities associated with subhalos depend on both their mass and the cluster-centric radius.
8. The tangential distortion signals, g_+ , in the range of ~ 0.02 – $2 h^{-1}$ Mpc show a complex structure which is well described by three mass components of the smooth mass distribution of the NFW model, subhalos, and LSS lensing model. Although the lensing signals are 1 order of magnitude lower than those for clusters at intermediate redshifts, $z \sim 0.2$ (Okabe et al. 2010b), the total S/N, $S/N \simeq 13.3$, is comparable to them or higher because of a correspondingly large number of background galaxies ($\sim 6 \times 10^5$). The S/Ns for subhalos and LSS lensing models are $S/N \simeq 4.4$ and $\simeq 1.3$, respectively. The 45° rotated component, g_\times , is consistent with a null signal.

We are grateful to N. Kaiser for developing the IMCAT package and making it publicly available. We thank Keiichi Umetsu, Masahiro Takada, Takashi Hamana, Eiichiro Komatsu, Yuki Okura, Neal Dalal, Marceau Limousin, Richard Massey, Hao-Yi Wu, Priya Natarajan, and Jean-Paul Kneib for helpful comments and/or discussions. We also thank Alan Lefor for English correction. This work was supported by World Premier International Research Center Initiative (WPI Initiative), MEXT, Japan.

APPENDIX A

ANISOTROPIC PSF CORRECTION

The anisotropic PSF correction is critically important for weak-lensing analysis of clusters with low lensing efficiency, such as the Coma cluster. Systematic residual ellipticities remaining after the correction will introduce a systematic bias in estimates of cluster and subhalo masses. We conducted five tests to assess the anisotropic PSF correction. As described in Section 2.2, we estimated $q_*^\alpha(\theta)$ patterns by fitting the stellar ellipticity components with the function of second-order bi-polynomials of the vector θ , and applied it to galaxy ellipticities.

To test the model, we first compared the observed $q_*^\alpha(\theta)$ distribution patterns with those of the model by rapidly alternating the two distributions on a monitor to allow visual identification of significant differences, since the human eye is sensitive to differences in rapidly changing images. We also investigated spatial distributions of the stellar ellipticity components, $e_*^\alpha(\theta)$, before and after the anisotropic PSF correction, as shown in Figure 17. Although there is a large-scale coherent pattern of raw stellar ellipticities (left panel of Figure 17), the residual stellar ellipticities after the correction visually confirmed the random distribution patterns (right panel of Figure 17).

Second, in order to more quantitatively assess the model, we computed an auto-correlation function for stellar ellipticities and a cross-correlation function for the ellipticities of galaxies and stars, before and after the correction, respectively. These are estimated by using the average for all pairs of galaxies/stars and stars separated by the angle θ , with equal weight. A clear positive correlation between observed stellar ellipticities is shown in the top-left panel of Figure 18. However, residual stellar ellipticities are suppressed to zero, even though they are slightly anti-correlated at a separation angle $\sim 1'$. Similarly, no correlation between the corrected galaxy and residual stellar ellipticities is found (right-middle panel of Figure 18). This test was conducted before applying the isotropic PSF correction, and the results support the conclusion that there is no systematic bias in the measurement of galaxy ellipticities.

Third, we investigated the cross-correlation function between residual stellar ellipticities and reduced shear g_α after the isotropic PSF correction and found the same result. Here, we plot the cross-correlation for our background sample after the color selection, estimated with a weight of w_g (Equation (3)), in the right-bottom panel of Figure 18. This plot clearly shows the null correlation and thus indicates that the systematic bias caused by imperfect PSF correction is negligible at most.

Fourth, we computed the median for two components of residual stellar ellipticities before and after the correction. The median for two components of residual stellar ellipticities after the anisotropic correction, $\bar{e}_{\text{res}}^* = (0.791 \pm 3.130, 1.127 \pm 2.331) \times 10^{-5}$, improves from those of raw stellar ellipticities before the correction, $\bar{e}_{\text{raw}}^* = (-1.179 \pm 0.014, -0.520 \pm 0.014) \times 10^{-2}$.

Fifth, we assessed the shape measurement using the same galaxies detected in all overlapping regions of different images (see also Section 2.2).

APPENDIX B

MAP MAKING

We reconstructed the projected mass distribution following Kaiser & Squires (1993). As described in detail in Okabe & Umetsu (2008), we pixelize the reduced shear into a regular grid with a Gaussian smoothing of $G(\theta) \propto \exp[-\theta^2/\theta_g^2]$. The resolution of the maps is defined by FWHM $\equiv 2\sqrt{\ln 2}\theta_g$. The smoothed shear pattern at an angular position θ is estimated as

$$\bar{g}_\alpha(\theta) = \frac{\sum_i G(\theta - \theta_i) w_{g,i} g_{\alpha,i}(\theta_i)}{\sum_i G(\theta - \theta_i) w_{g,i}} \quad (\text{B1})$$

where w_g and $g_{\alpha,i}$ are the statistical weight of Equation (3) and the reduced shear of the i th galaxy, respectively. The error variance for the smoothed shear (B1) is given by

$$\sigma_g^2(\theta) = \frac{\sum_i G(\theta - \theta_i)^2 w_{g,i}^2 \sigma_{g,i}^2}{\left(\sum_i G(\theta - \theta_i) w_{g,i}\right)^2}. \quad (\text{B2})$$

Then, the smoothed shear field (B1) is inverted with the kernel (Kaiser & Squires 1993) in Fourier space to obtain the projected mass distribution, $\kappa(\theta)$. Here, we assume the weak-limit of $g_\alpha = \gamma_\alpha/(1 - \kappa) \approx \gamma_\alpha$. We also compute a map of the significance level for mass reconstruction, $\nu(\theta) \equiv \kappa/\sigma_\kappa$, with the mass reconstruction error $\sigma_\kappa(\theta)$. We also make maps of luminosity ($l(\theta)$) and number density ($n(\theta)$) for member galaxies defined in Section 2.5 and the convergence field ($\kappa_{\text{LSS}}(\theta)$) of LSS lensing in Section 2.6 with a statistical weight of $w_{g,i} = 1$.

APPENDIX C

MODEL-INDEPENDENT MASS MEASUREMENT

A parameter-free estimation of subhalos is given by the aperture-densitometry, or the so-called ζ_c -statistics (Clowe et al. 2000). The projected mass, $M_{\zeta_c}(< \theta)$, is given by

$$M_{\zeta_c}(< \theta) = \pi \theta^2 \Sigma_{\text{cr}} \zeta_c(\theta, \theta_{\text{inn}}, \theta_{\text{out}}), \quad (\text{C1})$$

$$\begin{aligned} \zeta_c(\theta; \theta_{\text{inn}}, \theta_{\text{out}}) &= \bar{\kappa}(< \theta) - \bar{\kappa}(\theta_{\text{inn}} < \theta < \theta_{\text{out}}) \\ &= 2 \int_{\theta}^{\theta_{\text{inn}}} d \ln \theta' \langle \gamma_+(\theta) \rangle \\ &\quad + \frac{2}{1 - \theta_{\text{inn}}^2/\theta_{\text{out}}^2} \int_{\theta_{\text{inn}}}^{\theta_{\text{out}}} d \ln \theta' \langle \gamma_+(\theta) \rangle \end{aligned} \quad (\text{C2})$$

where θ_{inn} and θ_{out} are the inner and outer radii of the background annulus. The $\langle \gamma_+ \rangle$ is an azimuthal average of the tangential component of the gravitational shear, which we take $\langle \gamma_+(\theta) \rangle \approx \langle g_+(\theta) \rangle$ in the weak limit. The uncertainty in ζ_c at θ_i is estimated as

$$\begin{aligned} \sigma_i^2 &= 4 \sum_{j=i}^{N_{\text{inn}}} \left(\frac{\Delta \theta_j}{\theta_j} \right)^2 \sigma_{g_+}^2(\theta_j) + \left(\frac{2}{1 - \theta_{\text{inn}}^2/\theta_{\text{out}}^2} \right)^2 \\ &\quad \times \sum_{i=N_{\text{inn}}}^{N_{\text{out}}} \left(\frac{\Delta \theta_j}{\theta_j} \right)^2 \sigma_{g_+}^2(\theta_j), \end{aligned} \quad (\text{C3})$$

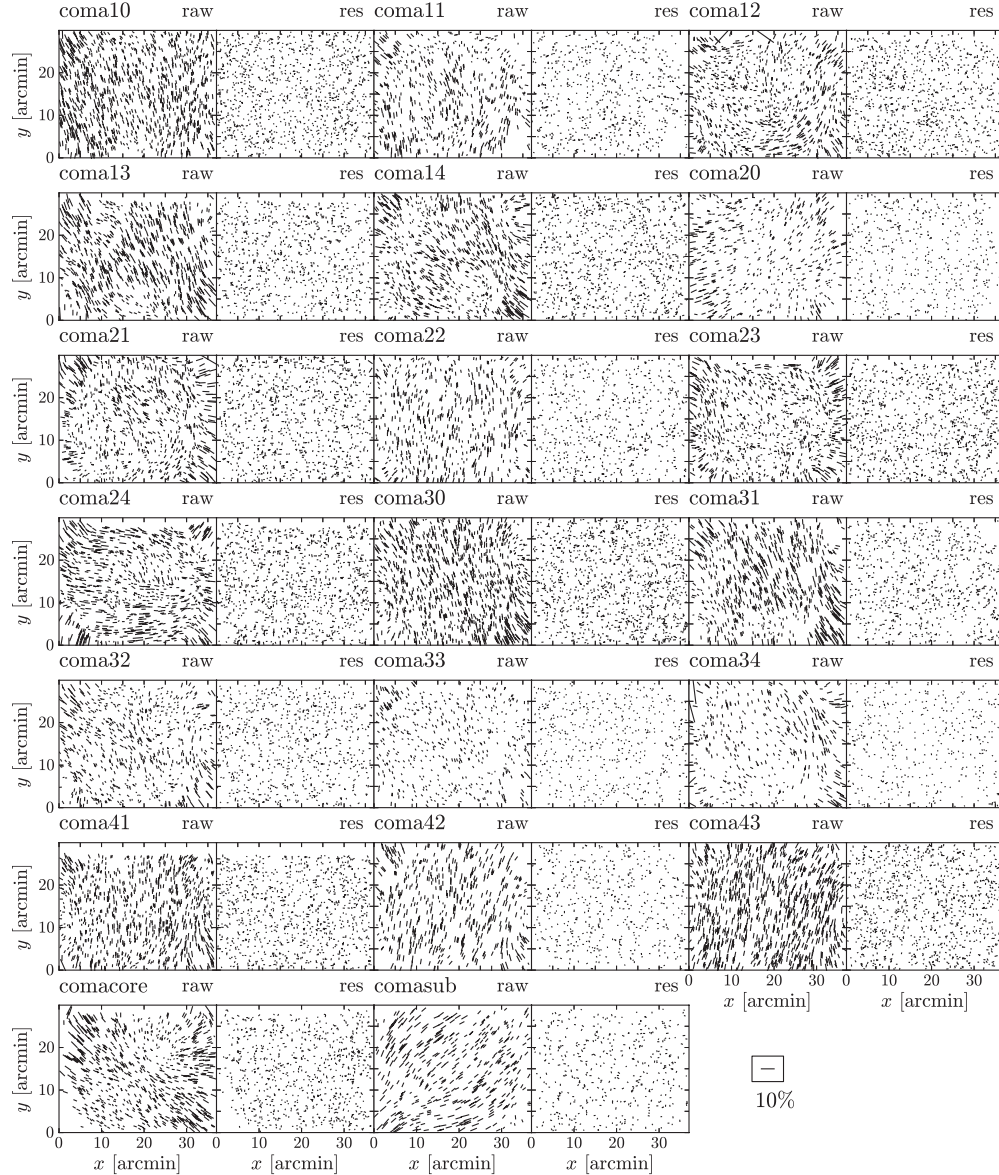


Figure 17. Pattern of stellar ellipticity before and after the anisotropic PSF correction for individual pointings. The data name is shown in the top left corner. The left and right panels show the raw ($e_{1,*}^{\text{raw}}, e_{2,*}^{\text{raw}}$) and residual ($e_{1,*}^{\text{res}}, e_{2,*}^{\text{res}}$) stellar ellipticities, respectively.

where N_{inn} and N_{out} are the indices for each of the discrete radial bins corresponding to the radii of θ_{inn} and θ_{out} in Equation (C1), respectively. An error covariance of ζ_c between each bin is given by $\sigma_{ij} = \sigma_{ji} = \sigma_j^2$ for $\theta_i < \theta_j$. The S/N of the radial profile, which is complementary information to that of peaks in mass maps, is computed by

$$S/N = \left(\sum_{ij} M_{\zeta_c,i} V_{ij}^{-1} M_{\zeta_c,j} \right)^{1/2} \quad (\text{C4})$$

where V_{ij}^{-1} is the inverse of the covariance matrix.

To quantify the mass of the subhalos, we estimate an average projected mass taking into account the error covariance matrix, as follows,

$$M_{2D} = \sum_{i=N_{s1}}^{N_{s2}} \Gamma_i M_{\zeta_c,i} \quad (\text{C5})$$

$$\sigma_{M_{2D}}^2 = \sum_{i,j=N_{s1}}^{N_{s2}} \Gamma_i \Gamma_j V_{ij} \quad (\text{C6})$$

$$\Gamma_i = \sum_{j=N_{s1}}^{N_{s2}} V_{ij}^{-1} / \sum_{i,j=N_{s1}}^{N_{s2}} V_{ij}^{-1} \quad (\text{C7})$$

where N_{s1} and N_{s2} are the indices for each of the discrete radii where M_{ζ_c} profile is saturated.

APPENDIX D

MASS MODELS

Mass models for cluster halos and subhalos are summarized in this section. Numerical simulations, based on the CDM model of structure formation, predicts that dark matter halos spanning a wide mass range can be described by a universal mass density profile (Navarro et al. 1996, 1997). In this paper, we refer to

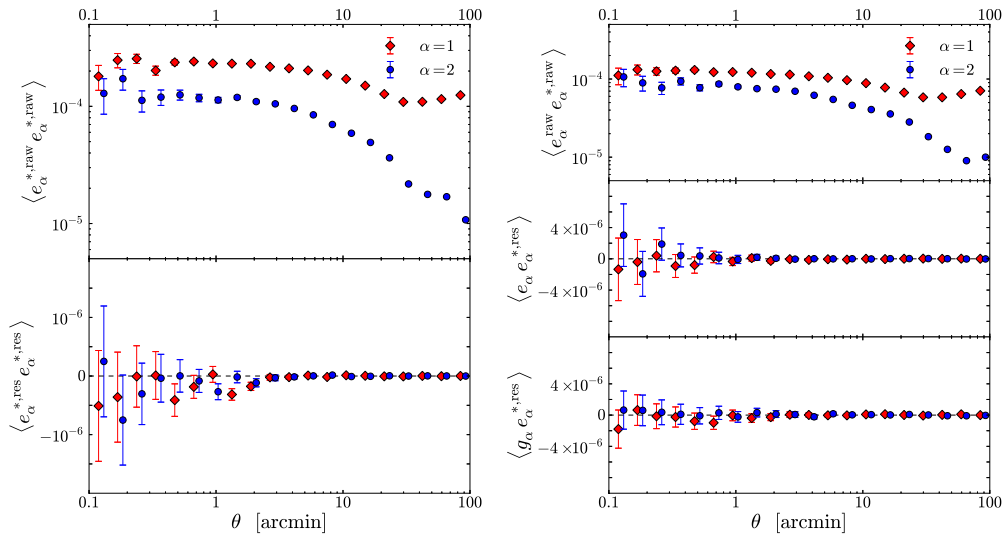


Figure 18. Auto correlation function for the stellar ellipticities (left) and a cross correlation function between the galaxy and stellar ellipticities (right) as a function of angular separation, θ . The red diamonds and blue circles denote two components of the ellipticity (e_{α} ; $\alpha = 1, 2$), respectively. The x positions for blue circles are shifted (multiplied by 1.1) from the originals. The raw stellar ellipticities are highly correlated (left-top panel), while the residual stellar ellipticities after the correction are consistent with zero (left-bottom panel). The cross correlation function between the raw galaxy and stellar ellipticities, $\langle e_{\alpha}^{\text{raw}} e_{\alpha}^{*,\text{raw}} \rangle$, shows positive values (right-top panel). The residual cross correlation function between the galaxy and stellar ellipticities, $\langle e_{\alpha} e_{\alpha}^{*,\text{res}} \rangle$, does not show any significant correlation over a wide range (right-middle panel). The cross correlation between the residual stellar ellipticities and the reduced shear for background galaxies which we used for lensing analysis, $\langle g_{\alpha} e_{\alpha}^{*,\text{res}} \rangle$, does not show any significant feature consistent with an imperfect anisotropic PSF correction (right-bottom panel).

(A color version of this figure is available in the online journal.)

these density profiles as the NFW profile which is expressed in the form of

$$\rho_{\text{NFW}}(r) = \frac{\rho_s}{(r/r_s)(1+r/r_s)^2}, \quad (\text{D1})$$

where ρ_s is the central density parameter and r_s is the scale radius. The density profile has inner and outer slope values of -1 and -3 , respectively. The three-dimensional spherical masses, M_{Δ} , enclosed by the radius, r_{Δ} , inside of which the mean density is Δ times the critical mass density, $\rho_{\text{cr}}(z)$, at the redshift, z , is given by

$$M_{\text{NFW}}(< r_{\Delta}) = \frac{4\pi\rho_s r_{\Delta}^3}{c_{\Delta}^3} \left[\ln(1+c_{\Delta}) - \frac{c_{\Delta}}{1+c_{\Delta}} \right]. \quad (\text{D2})$$

The NFW profile is specified by the two parameters including M_{Δ} and the halo concentration $c_{\Delta} = r_{\Delta}/r_s$.

Subhalo sizes are determined by the strong tidal field of the main cluster halo. The mass density outside the instantaneous tidal radius of subhalos drastically decreases and is close to zero due to tidal stripping (e.g., Tormen et al. 1998; Hayashi et al. 2003; Oguri & Lee 2004; Taylor & Babul 2004; van den Bosch et al. 2005). Therefore, the mass model for subhalos requires an additional parameter of the truncation radius, r_t . We consider two models of the truncation model for NFW and SIS models described above. We refer to these truncation models as the truncated NFW (TNFW; Takada & Jain 2003; Hamana et al. 2004). The interior mass density profile for the TNFW model follows the NFW model but is zero outside the truncation radius.

$$\begin{aligned} \rho_{\text{TNFW}}(r) &= \rho_{\text{NFW}}(r \leq r_t), \\ &= 0(r > r_t). \end{aligned} \quad (\text{D3})$$

This is an extreme case of the truncation model. The TNFW model (Okabe et al. 2010a) is specified by three parameters including the subhalo mass (M_t), a truncation radius (r_t) and a concentration (c_t). The slope of the lensing profile for the

TNFW model drastically changes outside the truncation radius and behaves as a point source ($\propto \theta^{-2}$). In model fitting, the truncation radius and the concentration are sensitive to this break and the inner profile, respectively. The subhalo mass is also determined by the distortion signal at the truncation radius. Since the mass densities outside the truncation radius are zero, the three- and two-dimensional masses within the truncation radius yield the exactly same value ($M_{3\text{D}} = M_{2\text{D}}$).

When we stack tangential distortion profiles for subhalos with different properties, the break in the distortion profile is smooth due to their intrinsic distribution. In addition to the TNFW model, we compute the model taking into account a distribution function of the truncation radius (TNFWProb). The probability function is assumed to be Gaussian, $p(r_t) = \exp(-\langle r_t - \langle r_t \rangle \rangle^2 / 2\sigma_r^2) / \sqrt{2\pi\sigma_r^2}$, where $\langle r_t \rangle$ and σ_r are the average and the standard error for the truncation radius, respectively. The mean lensing signal is expressed in terms of $\int p(r_t) g_+^{(\text{TNFW})} dr_t$. We do not assume a distribution over the subhalo mass but instead estimate the mean subhalo mass, $\langle M_t \rangle$, which is sensitive to a lensing signal at $\langle r_t \rangle$.

REFERENCES

- Adami, C., Biviano, A., Durret, F., & Mazure, A. 2005, *A&A*, **443**, 17
 Adami, C., Le Brun, V., Biviano, A., et al. 2009, *A&A*, **507**, 1225
 Andrade-Santos, F., Nulsen, P. E. J., Kraft, R. P., et al. 2013, *ApJ*, **766**, 107
 Angulo, R. E., Lacey, C. G., Baugh, C. M., & Frenk, C. S. 2009, *MNRAS*, **399**, 983
 Applegate, D. E., von der Linden, A., Kelly, P. L., et al. 2012, arXiv:1208.0605
 Bartelmann, M., & Schneider, P. 2001, *PhR*, **340**, 291
 Bertin, E., & Arnouts, S. 1996, *A&AS*, **117**, 393
 Boselli, A., & Gavazzi, G. 2006, *PASP*, **118**, 517
 Briel, U. G., Henry, J. P., & Boehringer, H. 1992, *A&A*, **259**, L31
 Broadhurst, T., Takada, M., Umetsu, K., et al. 2005, *ApJL*, **619**, L143
 Bullock, J. S., Kolatt, T. S., Sigad, Y., et al. 2001, *MNRAS*, **321**, 559
 Cappellari, M., Bacon, R., Bureau, M., et al. 2006, *MNRAS*, **366**, 1126
 Clowe, D., Luppino, G. A., Kaiser, N., & Gioia, I. M. 2000, *ApJ*, **539**, 540
 Cody, A. M., Carter, D., Bridges, T. J., Mobasher, B., & Poggianti, B. M. 2009, *MNRAS*, **396**, 1647

- Conselice, C. J., & Gallagher, J. S., III. 1999, *AJ*, 117, 75
- Cooray, A., & Sheth, R. 2002, *PhR*, 372, 1
- De Lucia, G., Kauffmann, G., Springel, V., et al. 2004, *MNRAS*, 348, 333
- Diemand, J., Moore, B., & Stadel, J. 2004, *MNRAS*, 352, 535
- Djorgovski, S., & Davis, M. 1987, *ApJ*, 313, 59
- Dressler, A., Lynden-Bell, D., Burstein, D., et al. 1987, *ApJ*, 313, 42
- Duffy, A. R., Schaye, J., Kay, S. T., & Dalla Vecchia, C. 2008, *MNRAS*, 390, L64
- Eisenstein, D. J., Weinberg, D. H., Agol, E., et al. 2011, *AJ*, 142, 72
- Gal, R. R., de Carvalho, R. R., Lopes, P. A. A., et al. 2003, *AJ*, 125, 2064
- Gan, J., Kang, X., van den Bosch, F. C., & Hou, J. 2010, *MNRAS*, 408, 2201
- Gao, L., De Lucia, G., White, S. D. M., & Jenkins, A. 2004a, *MNRAS*, 352, L1
- Gao, L., Navarro, J. F., Frenk, C. S., et al. 2012, *MNRAS*, 425, 2169
- Gao, L., White, S. D. M., Jenkins, A., Stoehr, F., & Springel, V. 2004b, *MNRAS*, 355, 819
- Gavazzi, R., Adami, C., Durret, F., et al. 2009, *A&A*, 498, L33
- Ghigna, S., Moore, B., Governato, F., et al. 2000, *ApJ*, 544, 616
- Giocoli, C., Pieri, L., & Tormen, G. 2008, *MNRAS*, 387, 689
- Giocoli, C., Tormen, G., Sheth, R. K., & van den Bosch, F. C. 2010, *MNRAS*, 404, 502
- Gregory, S. A., & Thompson, L. A. 1978, *ApJ*, 222, 784
- Guzik, J., & Seljak, U. 2002, *MNRAS*, 335, 311
- Hamana, T., Miyazaki, S., Shimasaku, K., et al. 2003, *ApJ*, 597, 98
- Hamana, T., Takada, M., & Yoshida, N. 2004, *MNRAS*, 350, 893
- Hao, J., McKay, T. A., Koester, B. P., et al. 2010, *ApJS*, 191, 254
- Hayashi, E., Navarro, J. F., Taylor, J. E., Stadel, J., & Quinn, T. 2003, *ApJ*, 584, 541
- Heymans, C., Van Waerbeke, L., Bacon, D., et al. 2006, *MNRAS*, 368, 1323
- Hinshaw, G., Larson, D., Komatsu, E., et al. 2013, *ApJS*, 208, 19
- Hoekstra, H. 2003, *MNRAS*, 339, 1155
- Hoekstra, H., Franx, M., & Kuijken, K. 2000, *ApJ*, 532, 88
- Hoekstra, H., Mahdavi, A., Babul, A., & Bildfell, C. 2012, *MNRAS*, 427, 1298
- Ichikawa, K., Matsushita, K., Okabe, N., et al. 2013, *ApJ*, 766, 90
- Ilbert, O., Capak, P., Salvato, M., et al. 2009, *ApJ*, 690, 1236
- Jeeson-Daniel, A., Dalla Vecchia, C., Haas, M. R., & Schaye, J. 2011, *MNRAS*, 415, L69
- Johnston, D. E., Sheldon, E. S., Wechsler, R. H., et al. 2007, arXiv:0709.1159
- Kaiser, N., & Squires, G. 1993, *ApJ*, 404, 441
- Kaiser, N., Squires, G., & Broadhurst, T. 1995, *ApJ*, 449, 460
- Kawaharada, M., Okabe, N., Umetsu, K., et al. 2010, *ApJ*, 714, 423
- Klypin, A. A., Trujillo-Gomez, S., & Primack, J. 2011, *ApJ*, 740, 102
- Koester, B. P., McKay, T. A., Annis, J., et al. 2007, *ApJ*, 660, 239
- Komatsu, E., Smith, K. M., Dunkley, J., et al. 2011, *ApJS*, 192, 18
- Kubo, J. M., Stebbins, A., Annis, J., et al. 2007, *ApJ*, 671, 1466
- Limousin, M., Kneib, J. P., Bardeau, S., et al. 2007, *A&A*, 461, 881
- Limousin, M., Kneib, J.-P., & Natarajan, P. 2005, *MNRAS*, 356, 309
- Limousin, M., Sommer-Larsen, J., Natarajan, P., & Milvang-Jensen, B. 2009, *ApJ*, 696, 1771
- Lokas, E. L., & Mamon, G. A. 2003, *MNRAS*, 343, 401
- Massey, R., Heymans, C., Bergé, J., et al. 2007, *MNRAS*, 376, 13
- McConnachie, A. W., Patton, D. R., Ellison, S. L., & Simard, L. 2009, *MNRAS*, 395, 255
- Mellier, Y., Mathez, G., Mazure, A., Chauvineau, B., & Proust, D. 1988, *A&A*, 199, 67
- Miyazaki, S., Komiyama, Y., Sekiguchi, M., et al. 2002, *PASJ*, 54, 833
- Nagai, D., & Kravtsov, A. V. 2005, *ApJ*, 618, 557
- Nagai, D., & Lau, E. T. 2011, *ApJL*, 731, L10
- Natarajan, P., De Lucia, G., & Springel, V. 2007, *MNRAS*, 376, 180
- Natarajan, P., Kneib, J.-P., Smail, I., et al. 2009, *ApJ*, 693, 970
- Natarajan, P., & Springel, V. 2004, *ApJL*, 617, L13
- Navarro, J. F., Frenk, C. S., & White, S. D. M. 1996, *ApJ*, 462, 563
- Navarro, J. F., Frenk, C. S., & White, S. D. M. 1997, *ApJ*, 490, 493
- Neumann, D. M., Arnaud, M., Gastaud, R., et al. 2001, *A&A*, 365, L74
- Oguri, M. 2010, *PASJ*, 62, 1017
- Oguri, M., Bayliss, M. B., Dahle, H., et al. 2012, *MNRAS*, 420, 3213
- Oguri, M., & Lee, J. 2004, *MNRAS*, 355, 120
- Oguri, M., & Takada, M. 2011, *PhRvD*, 83, 023008
- Oguri, M., Takada, M., Okabe, N., & Smith, G. P. 2010, *MNRAS*, 405, 2215
- Okabe, N., Bourdin, H., Mazzotta, P., & Maurogordato, S. 2011, *ApJ*, 741, 116
- Okabe, N., Okura, Y., & Futamase, T. 2010a, *ApJ*, 713, 291
- Okabe, N., Smith, G. P., Umetsu, K., Takada, M., & Futamase, T. 2013, *ApJL*, 769, L35
- Okabe, N., Takada, M., Umetsu, K., Futamase, T., & Smith, G. P. 2010b, *PASJ*, 62, 811
- Okabe, N., & Umetsu, K. 2008, *PASJ*, 60, 345
- Ouchi, M., Shimasaku, K., Okamura, S., et al. 2004, *ApJ*, 611, 685
- Planck Collaboration, Ade, P. A. R., Aghanim, N., et al. 2013, *A&A*, 554, 140
- Rines, K., Geller, M. J., Kurtz, M. J., & Diaferio, A. 2003, *AJ*, 126, 2152
- Sato, T., Sasaki, T., Matsushita, K., et al. 2012, *PASJ*, 64, 95
- Schechter, P. 1976, *ApJ*, 203, 297
- Schneider, P., van Waerbeke, L., Jain, B., & Kruse, G. 1998, *MNRAS*, 296, 873
- Seljak, U. 2000, *MNRAS*, 318, 203
- Shaw, L. D., Weller, J., Ostriker, J. P., & Bode, P. 2006, *ApJ*, 646, 815
- Simionescu, A., Werner, N., Urban, O., et al. 2013, *ApJ*, 775, 4
- Skibba, R. A., & Macciò, A. V. 2011, *MNRAS*, 416, 2388
- Skrutskie, M. F., Cutri, R. M., Stiening, R., et al. 2006, *AJ*, 131, 1163
- Smith, R. J., Lucey, J. R., Price, J., Hudson, M. J., & Phillipps, S. 2012, *MNRAS*, 419, 3167
- Springel, V., White, S. D. M., Tormen, G., & Kauffmann, G. 2001, *MNRAS*, 328, 726
- Takada, M., & Jain, B. 2003, *MNRAS*, 340, 580
- Taylor, J. E., & Babul, A. 2004, *MNRAS*, 348, 811
- Taylor, J. E., & Babul, A. 2005a, *MNRAS*, 364, 515
- Taylor, J. E., & Babul, A. 2005b, *MNRAS*, 364, 535
- Taylor, J. E., Massey, R. J., Leauthaud, A., et al. 2012, *ApJ*, 749, 127
- Tormen, G., Diaferio, A., & Syer, D. 1998, *MNRAS*, 299, 728
- Tormen, G., Moscardini, L., & Yoshida, N. 2004, *MNRAS*, 350, 1397
- Tozzi, P., & Norman, C. 2001, *ApJ*, 546, 63
- Umetsu, K., & Broadhurst, T. 2008, *ApJ*, 684, 177
- Umetsu, K., Broadhurst, T., Zitrin, A., et al. 2011, *ApJ*, 738, 41
- Umetsu, K., Medezinski, E., Broadhurst, T., et al. 2010, *ApJ*, 714, 1470
- Vale, A., & Ostriker, J. P. 2004, *MNRAS*, 353, 189
- van den Bosch, F. C., Tormen, G., & Giocoli, C. 2005, *MNRAS*, 359, 1029
- van den Bosch, F. C., Yang, X., & Mo, H. J. 2003, *MNRAS*, 340, 771
- van Uitert, E., Hoekstra, H., Velander, M., et al. 2011, *A&A*, 534, A14
- Walker, S. A., Fabian, A. C., Sanders, J. S., George, M. R., & Tawara, Y. 2012, *MNRAS*, 422, 3503
- Wen, Z. L., Han, J. L., & Liu, F. S. 2009, *ApJS*, 183, 197
- White, S. D. M., Briel, U. G., & Henry, J. P. 1993, *MNRAS*, 261, L8
- Wong, A. W. C., & Taylor, J. E. 2012, *ApJ*, 757, 102
- Wu, H.-Y., Hahn, O., Wechsler, R. H., Behroozi, P. S., & Mao, Y.-Y. 2013, *ApJ*, 767, 23
- Yagi, M., Kashikawa, N., Sekiguchi, M., et al. 2002, *AJ*, 123, 66
- Yang, X., Mo, H. J., van den Bosch, F. C., et al. 2006, *MNRAS*, 373, 1159
- Zabludoff, A. I., & Mulchaey, J. S. 1998, *ApJ*, 496, 39
- Zentner, A. R., Berlind, A. A., Bullock, J. S., Kravtsov, A. V., & Wechsler, R. H. 2005, *ApJ*, 624, 505